The Astrophysical Journal, 619:755–778, 2005 February 1

MODELING THE PAN–SPECTRAL ENERGY DISTRIBUTION OF STARBURST GALAXIES. I. THE ROLE OF ISM PRESSURE AND THE MOLECULAR CLOUD DISSIPATION TIMESCALE

Michael A. Dopita, Brent A. Groves, Jörg Fischera, and Ralph S. Sutherland
Research School of Astronomy and Astrophysics, Australian National University, Cotter Road, Weston Creek, ACT 2611, Australia; Michael.Dopita@anu.edu.au

Richard J. Tuffs and Cristina C. Popescu
Max-Plank-Institut für Kernphysik, Saupfercheckweg 1, D-69117 Heidelberg, Germany

Lisa J. Kewley
Harvard-Smithsonian Center for Astrophysics, 60 Garden Street, Cambridge, MA 02138

Michiel Reuland
Sterrewacht Leiden, P.O. Box 9513, 2300 RA Leiden, Netherlands

and

Claus Leitherer
Space Telescope Science Institute, 3700 San Martin Drive, Baltimore, MD 21218
Received 2004 April 2; accepted 2004 June 17

ABSTRACT

In this paper, we combine the stellar spectral synthesis code STARBURST99, the nebular modeling code MAPPINGS IIIq, a one-dimensional dynamical evolution model of H II regions around massive clusters of young stars, and a simplified model of synchrotron emissivity to produce purely theoretical self-consistent synthetic spectral energy distributions (SEDs) for (solar metallicity) starbursts lasting $\sim 10^8$ yr. These SEDs extend from the Lyman limit to beyond 21 cm. We find that two ISM parameters control the form of the SED: the pressure in the diffuse phase of the ISM (or, equivalently, its density), and the molecular cloud dissipation timescale. In particular, the shape of the far-infrared (dust re-emission) bump is strongly dependent on the mean pressure in the star-forming or starburst galaxy. This can explain the range of far-infrared (FIR) colors seen in starburst galaxies. In the case of objects of composite excitation, such diagrams potentially provide a means of estimating the fraction of the FIR emission that is contributed by an active nucleus. We present detailed SED fits to Arp 220 and NGC 6240, and we give the predicted colors for starburst galaxies derived from our models for the *IRAS* and the *Spitzer Space Telescope* MIPS and IRAC instruments. Our models reproduce the spread in observed colors of starburst galaxies. From both the SED fits and the color : color diagrams, we infer the presence of a population of compact and ultracompact H II regions around single OB stars or small OB clusters. Finally, we present absolute calibrations to convert observed fluxes into star formation rates in the UV (*GALEX*), at optical wavelengths (Hα), and in the IR (*IRAS* or *Spitzer*). We show that 25 μm fluxes are particularly valuable as star formation indicators, since they largely eliminate one of the parameters controlling the IR SED.

Subject headings: dust, extinction — galaxies: general — galaxies: starburst — H II regions — infrared: galaxies — radio continuum: galaxies — ultraviolet: galaxies

Online material: color figures, machine-readable tables

1. INTRODUCTION

A knowledge of the star formation rate (SFR) is fundamental if we are to understand the formation and evolution of galaxies. In a much-cited seminal paper, Madau et al. (1996) connected the star formation in the distant universe to that estimated from low-redshift surveys, by plotting the estimated star formation rate per unit comoving volume against redshift. A wide variety of techniques contribute toward populating this diagram with observational points.

At present, an unacceptable degree of uncertainty still attaches to the Madou plot, and hence to our overall understanding of the evolution of star formation in the universe. This is largely the result of the effects of dust obscuration in and around the star-forming regions, which are particularly severe for those techniques which depend on optical or UV data (see the review by Calzetti 2001). Use of the far-infrared (FIR) may provide improved estimates (Dwek et al. 1998; Gispert et al. 2000). Nonetheless, uncertainties still remain, since to derive these rates, one must assume that the dust is effectively acting as a bolometer wrapped around the star-forming region, and that cool and old stars do not provide too much of a contribution. All of these assumptions deserve closer examination in both disk and starburst galaxies.

A further major uncertainty relates to the fact that we do not yet have reliable and self-consistent theoretical spectral energy distributions (SEDs) covering the full range of the electromagnetic spectrum. In principle, almost any part of the SED of a starburst can be used as a star formation indicator, provided that the appropriate bolometric correction to the absolute luminosity can be made. These bolometric corrections critically depend on the dust absorption and the geometry of the dust clouds, both optically thin and optically thick, with respect to both the ionizing stars and the older stellar population.

In principle, provided that the initial mass function (IMF) is invariant, the intrinsic UV luminosity should scale directly as the star formation rate. From stellar spectral synthesis models, the star formation rate is given in terms of the 1500 Å flux by (Kennicutt 1998; Panuzzo et al. 2003)

$$\frac{\mathrm{SFR_{UV}}}{M_\odot\ \mathrm{yr}^{-1}} = (1.2\text{–}1.4)\times 10^{-28}\frac{L_{\mathrm{UV}}}{\mathrm{ergs\ s^{-1}\ Hz^{-1}}}. \quad (1)$$

In practice, the results obtained with this technique depend critically on the corrections needed to account for the dust in and around the star-forming galaxy. These are very uncertain; there are claims that a typical $z = 3$ galaxy suffers a factor of 10 extinction at a wavelength of 1500 Å in the rest frame of the galaxy (Meurer et al. 1999; Sawicki & Yee 1998). Others argue for more modest corrections (e.g., Trager et al. 1997). In normal galaxies, Bell & Kennicutt (2001) find that although mean extinctions are modest (about 1.4 mag at 1550 Å), the scatter from galaxy to galaxy is very large. For individual galaxies at high redshift the reddening and the SFR are strongly correlated, and since many fainter galaxies at high redshift are missed completely, potentially large uncertainties exist in the derived star formation rates (Adelberger & Steidel 2000).

A fairly direct and extensively used technique is to measure hydrogen recombination line fluxes (Bell & Kennicutt 2001; Gallego et al. 1995; Jones & Bland-Hawthorn 2001; Moorwood et al. 2000; Tresse & Maddox 1998; Pascual et al. 2001; Yan et al. 1999; Dopita et al. 2002b, to name but a few). Provided that the H II region can absorb all the extreme-ultraviolet (EUV) photons produced by the central stars, this should be a reliable technique, since in this case the flux in any hydrogen line is simply proportional to the number of photons produced by the hot stars, which is in turn proportional to the birthrate of massive stars. This relationship has been well calibrated at solar metallicity for the Hα line. In units of $M_\odot\ \mathrm{yr}^{-1}$, the estimated star formation rate is given by (Dopita & Ryder 1994; Kennicutt 1998; Panuzzo et al. 2003)

$$\frac{\mathrm{SFR_{H\alpha}}}{M_\odot\ \mathrm{yr}^{-1}} = (7.0\text{–}7.9)\times 10^{-42}\frac{L_{\mathrm{H\alpha}}}{\mathrm{ergs\ s^{-1}}}. \quad (2)$$

Provided that the star formation regions are resolved, their Balmer decrements can be used to estimate the absorption in any foreground dust screen. However, it is possible that some star-forming regions are completely obscured, even at Hα. This problem can be avoided by observing at infrared wavelengths, in Brα, for example. A further complication is that the dust content of the nebula is metallicity-dependent, and therefore an appreciable fraction of the hydrogen ionizing photons may be absorbed by dust in high-metallicity H II regions. This possibility, first seriously quantified by Petrosian et al. (1972), has been discussed by a number of authors since (Panagia 1974; Mezger et al. 1974; Natta & Panagia 1976; Sarazin 1977; Smith et al. 1978; Shields & Kennicutt 1995; Bottorff et al. 1998). Its effect has been investigated and quantified (as far as is possible by direct observation) in a series of recent papers by Inoue and collaborators (Inoue et al. 2000, 2001; Inoue 2001). Dopita et al. (2003) has shown that this effect increases in importance in the more compact H II regions, and may lead to errors as high as ~30% in the estimated SFR.

In the case of dusty starburst galaxies, the total 80–1000 μm infrared luminosity, L_{IR}, as measured in the rest-frame frequency of the galaxy, can be used to estimate the total SFR (Kennicutt 1998; Panuzzo et al. 2003),

$$\frac{\mathrm{SFR_{IR}}}{M_\odot\ \mathrm{yr}^{-1}} = (4.5\text{–}4.6)\times 10^{-44}\frac{L_{\mathrm{IR}}}{\mathrm{ergs\ s^{-1}}}. \quad (3)$$

In deriving the proportionality between IR flux and SFR, it is generally assumed that the dust acts as a sort of "bolometer," wrapped around the star formation regions, and re-emitting most, if not all, the incident EUV and FUV photons. In practice, this is one of the many "geometrical" factors that render the derivation of the SFR quite uncertain. For example, Inoue (2002) includes a number of these geometrical factors in the formula for the IR luminosity of a galaxy,

$$L_{\mathrm{IR}} = L_{\mathrm{Ly\alpha}} + (1-f)L_{\mathrm{LC}} + \epsilon L_{\mathrm{UV}} + \eta L_{\mathrm{old}}. \quad (4)$$

This allows a fraction $(1-f)$ of the ionizing flux to be absorbed by dust in the H II region, assumes that all of the Lyα photons are multiply scattered by the gas and ultimately absorbed by dust in the surrounding H I region, that a fraction ϵ of the nonionizing UV photons are absorbed, and that a fraction η of the radiation field produced by the old stars is also absorbed by dust. Photoionization models of H II regions show that, typically, the Lyα flux is of the order of 30% of the total stellar flux absorbed by the nebula, so that globally, the dust is fairly efficient in capturing and reradiating the flux originally radiated by the star in the Lyman continuum. Indeed, since most of the FIR flux results from the absorption of both the nonionizing and ionizing photons in the photodissociation regions around H II regions, and since the temperature of the dust depends critically on the distance of the dust from the stars, it is clear that a good understanding of the geometry of the dusty H I and molecular gas with respect to newly born stars is critical to our understanding of the SED.

In combination with STARBURST99 (Leitherer et al. 1999) modeling, Hirashita et al. (2003) have applied equation (4) to the observations of star-forming galaxies in order to estimate the empirical values for the geometrical factors, which provide estimates for SFRs consistent between the UV, IR, and Hα estimators.

Recently, several very sophisticated approaches to the determination of the SED in galaxies have been developed. For normal galaxies the models of Silva et al. (1998) explicitly allow for the clumpy distribution of dust, strongly spatially correlated with the UV-emitting young stellar clusters, and probably associated with the dense molecular clouds from which the young stars have been formed. The model of Popescu et al. (2000), subsequently extended in later papers (Misiriotis et al. 2001; Tuffs et al. 2004), explicitly takes into account the three-dimensional structure of spiral galaxies in terms of both their stellar, gas and dust distributions to provide projected photometric properties and attenuation characteristics.

For starburst galaxies, Hirashita & Ferrara (2002) and Takeuchi et al. (2003) have developed a dust re-emission model appropriate to low-metallicity young galaxies at high redshift. Tagaki et al. (2003a, 2003b) have developed a mathematically elegant spherically symmetric radiative transfer model that includes the very important temperature fluctuations of the small grain populations and emission in the polycyclic aromatic hydrocarbon (PAH) features between 3 and 30 μm. Applied to starburst systems, this model suggests that star formation rates are positively correlated with the structural characteristics of the

star-forming region: regions of high star formation rate are both compact and highly obscured at optical wavelengths.

Because of their effect both on the efficiency of the production of IR emission and on the form of the IR emission through the dust temperature distribution, these geometrical factors largely determine the FIR SED. In a pair of recent papers Dale and coworkers have used *Infrared Space Observatory* (*ISO*) observations to develop a (largely empirical) family of templates to fit the variety of the forms of the IR SED (Dale et al. 2001; Dale & Helou 2002). This work assumes a power-law distribution of dust mass with local radiation field intensity to provide a wide range of dust temperatures. It appears to indicate that the SEDs of star-forming galaxies could fit to a one-parameter family of curves determined essentially by the exponent, α, of the power-law distribution of the dust masses with the radiation field intensity, where the radiation field is assumed to have the color of the local interstellar radiation field. This will not be the case in starburst galaxies, where the radiation field will be harder than the local interstellar radiation field, and where the geometry of the dust with respect to the gas is determined by the evolution of H II regions. It also may not be applicable even in normal galaxies, which are known through direct observation to appear as the superposition of different geometrical components whose dust emission has different intensities and colors (Tuffs & Popescu 2003). The commonly used 60/100 μm color diagnostic cannot be interpreted in terms of a single grain emission component, since the 60 μm emission is seen to come mainly from warm dust locally heated in H II regions, while the 100 μm emission comes both from the H II regions and the cold diffuse interarm emission.

In this paper, we attempt to provide a theoretical approach to the generation of pan–spectral energy distributions in the context of starburst galaxies. This provides physical insight into how the geometrical factors discussed above are determined largely by the temporal evolution of the H II region complexes in starburst galaxies. We have included the dust physics and radiative transfer both in the ionized H II plasma and in the dense molecular clouds associated with them. In particular, we show that the stochastic average pressure within the star formation region plays a major role in determining the FIR SED through its effect on the grain temperature, and that the rate at which the molecular clouds are dispersed and destroyed by the expanding H II complexes is fundamental to our understanding of the geometrical factors that affect the global SED.

This paper is organized as follows. In § 2 we describe the STARBURST99 modeling, which provides the input stellar spectra, and in § 3 we uses the mechanical energy input given by the STARBURST99 modeling to build a simple one-dimensional temporal evolution model for the H II regions surrounding a typical OB stellar cluster. In § 4 we describe the dust model used in this model, and show how the photodissociation of PAH molecules combined with a turbulent ISM may explain the observed attenuation curve of starburst galaxies. The MAPPINGS IIIq (Sutherland & Dopita 1993; Dopita et al. 2002a) modeling of the emission line, atomic continuum, and dust re-emission spectrum of these H II regions and their surrounding photodissociation regions (PDRs) and the generation from these models of the global starburst SEDs is described in § 7. In § 8 we discuss the parameters that have a controlling influence of the form of the theoretical SEDs, and go on to compare the models with observations in § 9. Finally, in § 10 we use the model to provide a theoretical recalibration of the various star formation indicators. In the conclusion, we enumerate the main results of the paper, and we emphasize the limitations of the models.

All the models presented in this paper have a solar abundance set. In Paper II of this series, we will investigate the effect of chemical abundance on the form of the SEDs.

2. STELLAR SPECTRAL SYNTHESIS MODELING

Starburst activity was first linked to galaxy interactions decades ago. In 1967, Sersic & Pastoriza (1967) found that galaxies harboring hotspots all had extreme blue colors in their centers, a property shared by the majority of interacting or peculiar galaxies in the Vorontsov-Velyaminov (1959) and Arp catalogs. An excess of radio emission was found in interacting galaxies, further strengthening the link between star formation and interaction (Sulentic 1976; Condon & Dressel 1978; Hummel 1980). Larson & Tinsley (1978) first suggested that tidal forces in interacting galaxies could trigger bursts of star formation. Since then, numerous studies have produced evidence for interaction-induced starburst activity (e.g., Petrosian et al. 1978; Condon et al. 1982; Keel et al. 1985; Madore 1986; Kennicutt et al. 1987; Bushouse 1987; Hummel et al. 1990; Donzelli & Pastoriza 1997; Barton et al. 2000; Petrosian et al. 2002; Lambas et al. 2003).

The typical duration of such interactions is a dynamical timescale, comparable to the orbital timescale of stars in the gravitational well of the system, $\sim 10^8$ yr. The details of the star formation triggered by such interactions depend on the many parameters of the interaction, such as the impact parameter, the relative velocities, the relative orientations of the spin axes, and the relative masses of the systems. Simulation of galactic mergers (Barnes & Hernquist 1996) suggests that the most violent star formation tends to be triggered in two separate episodes: during the initial collision of the systems and later, when tidal tail debris rains down into the nuclear regions of the merged systems. Enhanced star formation can occur throughout the interaction.

Given that each case will be different, for simplicity, here we have assumed that in our model starbursts, stars are being created continuously as separated 10^4 $M_\odot$ clusters scattered through the same volume, so as to give a mean star formation rate of 1 $M_\odot$ yr^{-1}. Thus, in the total lifetime of the starburst, 10^8 yr, some 10^4 such clusters will be formed.

Clusters of young stars are dust-enshrouded for the first $\sim$1–2 Myr, and produce the majority of their ionizing UV photons within the first $\sim$4–6 Myr of their lifetime. Thus star formation indicators based on nebular emission lines such as Hα or [O II], or else based on dust re-emission processes such as the 60 μm continuum flux, are strongly biased toward measuring recent star formation rates. In contrast, features that more directly measure the older population or the total luminosity, such as the near-IR continuum or the PAH emission features, measure the star formation rates integrated over somewhat longer periods. Assumptions about the total duration of the starburst do not greatly affect the calibration of the star formation rates based on either the UV, emission line, or FIR SED; the total luminosity of starburst increases by only by 10% between 5×10^7 and 10^8 yr according to the STARBURST99 models (Leitherer et al. 1999).

We have used the most recent version of the STARBURST99 code to generate the theoretical stellar SEDs of

1. instantaneous starbursts, sampled at 1 Myr age intervals from 0 Myr up to 10 Myr; and
2. continuous star formation at the rate of 1 $M_\odot$ yr^{-1} up to a maximum age of 10^8 yr.

These models assume solar metallicity, a standard Salpeter initial mass function, and upper and lower mass cutoffs of 120 and 1 $M_\odot$, respectively, on the zero-age main sequence. The

stellar atmosphere models for stars with plane-parallel atmospheres are based on the Kurucz (1992) models as compiled by Lejeune et al. (1997). The fully line-blanketed Wolf-Rayet atmosphere models of Hillier & Miller (1998) and the non-LTE O-star atmospheres of Pauldrach et al. (2001) have been incorporated into STARBURST99 as described in Smith et al. (2002). We use the full suite of atmosphere models to provide the most up-to-date stellar radiation field possible. All STARBURST99 models were rebinned to the lower spectral resolution input energy bins required by MAPPINGS IIIq.

The instantaneous burst models were used as the input spectra for the H II region nebular gas and dust modeling, while the continuous star formation models form a theoretical global SED for the older stars with ages between 11 and 100 Myr. The contribution of the older stars was distributed between the H II regions of different ages in proportion to their volume, and added to the stellar SEDs of the young cluster, which principally excite the H II regions. Thus our global SED is composed of the sum of all the contributions from the stars and their surrounding H II regions, which provide an average star formation rate of 1 $M_\odot$ yr^{-1} for a total time of 10^8 yr, finely sampled in time at 1 Myr time intervals between 0 and 10 Myr.

3. THE DYNAMICAL EVOLUTION OF H II REGIONS

It is very easy to understand why the temporal evolution of the H II regions surrounding young clusters of stars might be quite important in influencing the SED of starburst galaxies. First, the inner radius, $R_{\rm in}$, of the ionized shell and the pressure in the H II region together determine the ionization parameter, $\mathcal{U} = F_*/4\pi c R_{\rm in}^2 n_{\rm H\,II}$, where F_* is the flux of ionizing photons from cluster stars, c is the speed of light, and $n_{\rm H\,II}$ is the particle density in the H II region. As is well understood from photoionization theory (see Dopita & Sutherland 2003), the emission line spectrum of an H II region is determined primarily by the effective temperature of the cluster stars (itself a function of time) and by the ionization parameter, which is determined by the radius : time and radius : pressure relationships. These relationships need to be derived from models of the dynamical evolution of the H II regions, and are determined by the deposition of mechanical energy and momentum from the stellar winds and by supernovae.

The FIR SED is also influenced by these parameters, because, provided the nonionizing UV is absorbed on a scale less than the radius of the H II region, the outer radius of the H II region largely determines the characteristic dust temperature for a given stellar luminosity, and the IR PAH features are generated mostly in the photodissociation region surrounding the H II region.

In essence, then, the evolution of the H II regions determines the geometry of the gas and the dust with respect to the hot stars, and these geometrical effects determine various aspects of the SED. These effects have not hitherto been taken into account in any self-consistent way in the computation of SEDs. The most sophisticated treatment so far can be found in the "semi-analytic" framework of Granato et al. (2000), Bressan et al. (2002), and Panuzzo et al. (2003). In this, the young stars are treated as escaping from a dense molecular cloud environment on a characteristic timescale that is environment-dependent. However, such a treatment cannot properly take into account either the change of ionization parameter within the H II regions nor the change in the mean dust temperature with time.

The theory of the size distribution of H II regions has been presented by Oey & Clarke (1997, 1998). According to these papers, the H II regions expand and evolve as mass-loss– and supernova-driven bubbles for as long as their internal pressure exceeds the ambient pressure in the ISM. When this condition is no longer met, the H II region is assumed to "stall." Of course, on reaching the stall condition, the H II region does not abruptly stop expanding, but a momentum-conserving expansion continues until interstellar turbulence destroys the integrity of swept-up shell. The time taken to reach the stall radius turns out to be proportional to the stall radius, and the mass of the OB star cluster is important in determining the stall radius; low-mass cluster H II regions stall early and at small radius.

This theory emphasizes the important role of the pressure in the ISM in determining the radius of an individual H II region and its evolution with time. In particular, with higher ISM pressure, the H II region stalls at smaller radius, and therefore the mean dust temperature in the atomic and molecular shell around the H II region should be higher in high-pressure environments. We would therefore expect the FIR SED to peak at shorter wavelengths in high-pressure starburst regions. It is this correlation that we seek to investigate in this paper.

According to the mass-loss–driven bubble theory of Weaver et al. (1977), the radius, R, and the internal pressure, P, of an H II region are given by (cf. eqs. [24] and [25] of Oey & Clarke 1997)

$$R = \left(\frac{250}{308\pi}\right)^{1/5} L_{\rm mech}^{1/5} \rho_0^{-1/5} t^{3/5}, \tag{5}$$

$$P = \frac{7}{(3850\pi)^{2/5}} L_{\rm mech}^{2/5} \rho_0^{3/5} t^{-4/5}, \tag{6}$$

where $L_{\rm mech}$ is the mechanical luminosity of the mass-loss from the central stars, ρ_0 is the density of the ambient medium, and t is the time. The particle density is given in terms of the ambient density by $n = \rho_0/\mu m_{\rm H}$, and the ambient pressure $P_0 = nkT_0$. Eliminating t between equations (5) and (6) and setting $P = P_0$, we obtain the following conditions for stall:

$$P = \frac{7}{(3850\pi)^{2/5}} \left(\frac{250}{308\pi}\right)^{4/15} \left(\frac{L_{\rm mech}}{\mu m_{\rm H} n}\right)^{2/3} \frac{\mu m_{\rm H} n}{R^{4/3}} \tag{7}$$

$$= nkT_0 = n_{\rm H\,II} k T_{\rm H\,II}. \tag{8}$$

These equations imply that, for any given pressure in the ISM, all stalled H II regions have a common ratio $L_{\rm mech}/n_{\rm H\,II}R^2$. Thus, to the extent that $F_* \propto L_{\rm mech}$, where F_* is the flux of ionizing photons from the central stars, then all stalled H II regions will be characterized by a common value of the ionization parameter, $\mathcal{U} = F_*/4\pi c R_{\rm in}^2 n_{\rm H\,II}$. In fact, the STARBURST99 models show that the ratio of mechanical luminosity to ionizing photons may vary by as much as a factor of 10 during the first 10^7 yr of evolution. Nonetheless, most observed extragalactic H II regions show a fairly limited range in their ionization parameters (Kewley & Dopita 2002), and most H II regions should be in the stall condition (Oey & Clarke 1997), so that the above argument may well represent the basis of a theoretical explanation of this curious observational result.

Although we have emphasized the role of pressure, equation (8) shows that the stall condition might be better cast as a relationship between radius and ambient density, since it is the ambient density that determines the expansion history of the bubble. The effective ambient density is set by the density of the phase of the ISM that has the largest volume filling factor. We have assumed that, in starburst galaxies, this phase is a warm ionized medium (WIM) or warm neutral medium (WNM) heated by the photons

and mechanical energy of the starburst itself. Since both of these phases have a temperature $T \sim 10^4$ K, they also have similar densities for a given pressure.

Whether or not the H II regions are in the stall condition, the observed ionization parameter provides an important constraint on the internal pressure, and, more importantly, on the radiation field density incident on photodissociation region (PDR) around the H II region. This determines the characteristic dust temperature, and hence the wavelength of the peak in the FIR dust reemission feature.

H II regions in the stalled condition are found preferentially in regions of higher ISM pressure or density, and around lower mass clusters. Here we consider the variation in pressure, but we have not taken into account the mass distribution of the central clusters, using instead a "representative" cluster of mass $10^4\ M_\odot$. Clearly, the cluster mass distribution is an important parameter, the investigation of which is deferred for a future paper.

In the stall condition the expansion of the bubble does not cease entirely. By the time the stall radius is reached there is already a massive shell of swept-up gas, and this carries a substantial momentum. In our evolutionary calculations, we have assumed that the evolution of the bubble subsequent to the stall condition being reached continues according to the momentum-conserving solution for the swept-up shell,

$$R = \left(\frac{3M_{\rm stall}v_{\rm stall}}{\pi\rho_0}\right)^{1/4} t^{1/4}, \tag{9}$$

where the mass and velocity of the swept-up shell at the stall radius are $M_{\rm stall}$ and $v_{\rm stall}$, respectively.

3.1. *Bubbles with Time-dependent Luminosity*

We have used the stellar wind and supernova power output for a $10^4\ M_\odot$ cluster as predicted by the STARBURST99 code to make a Runge-Kutta integration of the equation of motion of the H II shell. The internal pressure is calculated from equation (8), with the instantaneous power output being smoothed over a period of 1 Myr to eliminate short-timescale pressure fluctuations.

For a time dependent wind+supernova mechanical luminosity $L_{\rm mech}(t)$ and an ambient medium density of ρ_0, the equations of conservation of mass, momentum, and energy for the mass M of the swept-up shell for a stellar wind bubble are

$$\frac{d}{dt}(M) = 4\pi R^2 \rho_0 \dot{R}, \tag{10}$$

$$\frac{d}{dt}\left(M\dot{R}\right) = 4\pi P R^2, \tag{11}$$

$$\frac{d}{dt}\left(PR^3\right) = \frac{L_{\rm mech}(t)}{2\pi} - 2PR^2\dot{R}, \tag{12}$$

where R is the outer shell radius. Here P is the bubble pressure, and $P \gg P_0$. By assuming that the bubble pressure is much greater than the ambient pressure, we have an energy-driven bubble. This will be true until shortly before the stall radius is reached.

Assuming that $\gamma = 5/3$ defines the equation of state of the bubble gas, we can combine these into a single differential equation, which is numerically integrated to allow for an arbitrary, time-dependent, mechanical luminosity L_w,

$$\frac{d}{dt}\left[R\frac{d}{dt}\left(R^3\dot{R}\right)\right] + \frac{9}{2}R^2\dot{R}^3 = \frac{3L_{\rm mech}(t)}{2\pi\rho_0}. \tag{13}$$

This equation was then integrated using a standard Runge-Kutta fourth-order integration with an adaptive step size, using the STARBURST 99-generated tabulated input mechanical energy luminosity for our cluster as a function of time until the stall condition was reached, after which the momentum-conserving solution was adopted (eq. [9]).

This simple integration does not yield results in accord with observations. The bubble expands to too large a diameter without reaching the stall condition, and the internal pressure is too high. As a result, the ionization parameter in the ionized shell is about a factor of 10 below the observed values for extragalactic H II regions as determined by Kewley & Dopita (2002) at all times during the lifetime of the bubble.

This problem can be rectified by assuming that the mechanical power output of the young stars is much less effective than the simple one-dimensional hydrodynamical models would suggest in terms of its efficiency in inflating the ionized bubble. Empirically, we determined that the effective power input of the stars would have to be decreased by a factor of 10 to ensure that the ionization parameter in the H II region matches the observed range of $3 \times 10^{-4} \leq U \leq 3 \times 10^{-3}$ (Kewley & Dopita 2002). This is in part due to the decrease in the radius of the bubble, and in part due to the lower internal pressure.

Interestingly enough, similar discrepancies between observation and the simple mass-loss bubble theory have emerged in analyses of the dynamics of bubbles and of their stellar content (García-Segura & Mac Low 1995; Oey 1996; Nazé et al. 2001). In these studies discrepancies of between 1 and 2 orders of magnitude have been noted. In all cases, the energy flux in the stellar winds predicted by the analysis of the stellar content exceeds the energy flux inferred from the dynamics. These discrepancies probably arise out of the limitations of the one-dimensional hydrodynamic models. Such models cannot take into account a number of effects that lead to a decreased efficiency in inflating the mass-loss bubble. These include enhanced radiative losses in the shocked stellar wind plasma through operation of the Vishniac instability, blowouts caused by the breakup of the atomic and molecular shell surrounding the H II region, and "poisoning" of the hot plasma through photoablation and entrainment of fragments within the hot shell.

In the light of this, we have modeled our $10^4\ M_\odot$ clusters as if they only had the mechanical energy luminosity of a $10^3\ M_\odot$ cluster. This ensures that our model H II regions have ionization parameters that accord with observations, and this will also ensure that the dust grains in the PDRs of these bubbles will be illuminated by a radiation field of the correct strength, so that the grains will have the correct temperatures.

In Figure 1 we plot the computed time evolution of the radius of the bubble as a function of the mean pressure P/k (measured in units of cm^{-3} K). The undisturbed gas outside the bubble is assumed to be part of the warm ionized medium, so that $P/k = 10^4$ corresponds to an atomic density of $\sim$1.0 cm^{-3}. In Figure 2 we plot the corresponding evolution of the internal pressure in the bubble, which can be identified as the pressure in the H II region. Note the peak in the pressure that appears near $\log t \sim 6.5$ yr, which corresponds to the onset of the energy input by Type II supernovae.

For $P/k < 10^6$ the bubble does not stall until quite late in its evolution, but for the highest pressures the stall condition is reached very early on. This ensures a large range in the final radii. Furthermore, for all the models, the pressure inside the bubble is quite strongly correlated with the external pressure, for times greater than about 1 Myr and up to the time at which the Type II supernova energy input switches off. This suggests

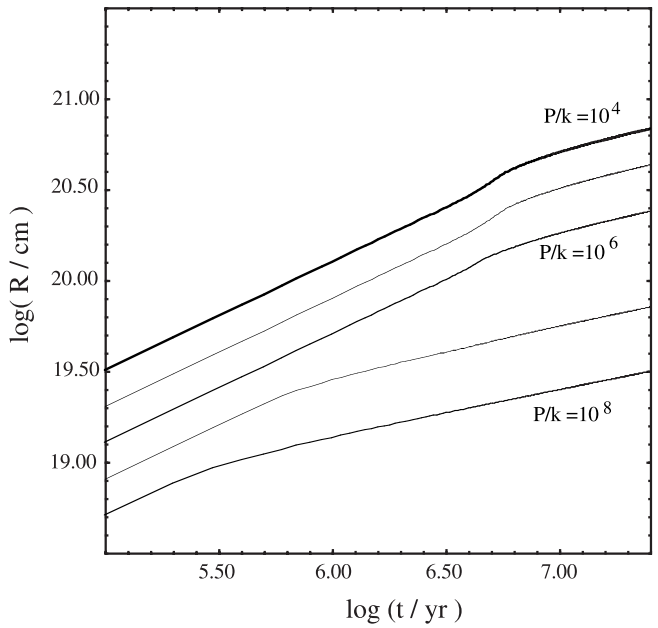

FIG. 1.—Time variation of the radius of the H II bubble as a function of the pressure in the ISM.

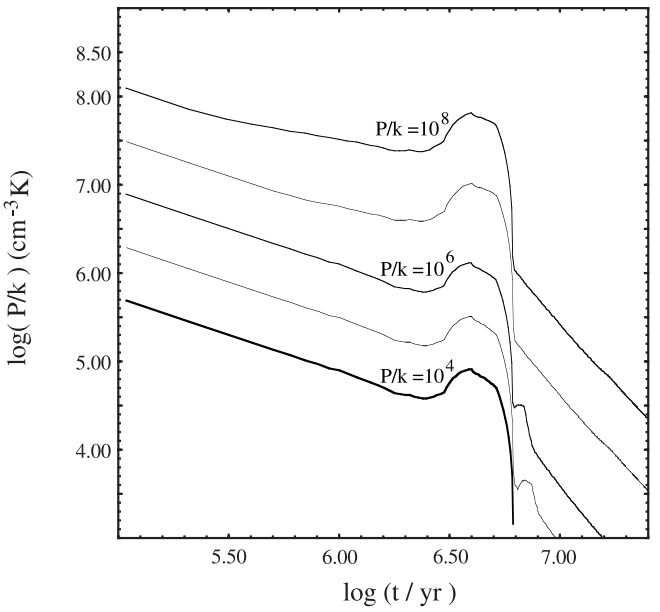

FIG. 2.—Time variation of the interior pressure of the H II bubble as a function of the pressure in the ISM.

that a measurement of the density in the ionized plasma using a density-sensitive ratio such as the [S II] $\lambda\lambda$6717/6731 could be used to help estimate the mean ambient ISM pressure in the star-forming region.

During the evolution of the H II bubble, the distribution of the radiation field within the bubble can be modified by the dynamical evolution of the central cluster, and indeed, by the turbulent breakup of the shell of gas around the H II region. For, example, at 10^7 yr the mean expansion speed of the H II bubble is 0.6, 5.7, and 17.3 km s^{-1} for $P_0/k = 10^8$,10^6, and 10^4 cm^{-3} K, respectively. Thus, at the higher pressures, the velocity dispersion of the stars in the central star cluster is likely to rival or exceed the expansion of the H II region, leading to a breakdown in the assumption that the illumination of the PDR at the edge of the bubble is from a single source at the center of the bubble. Under such circumstances, the rate of expansion of the bubble can be determined by the velocity dispersion of the stars rather than the hydrodynamical effects, with the "bubble" in fact being a cluster of smaller H II regions from individual stars, rather than a single cavity. In this case, the picture might be of a molecular cloud being excavated from within through the growth of independent H II regions inflated by single stars (or by small numbers of stars), eventually creating a porous parent molecular cloud.

All of this serves to highlight the fact that the time has come to abandon the simple one-dimensional evolutionary hydrodynamic model in favor of an approach that properly takes into account both the dynamics of the central cluster and the hydrodynamics of both the ionized and the molecular gas. This treatment is beyond the scope of this paper.

4. TREATMENT OF DUST AND PAH PHYSICS

4.1. *The PAH Molecules*

The numerous emission features in the 3–30 μm region, formerly referred to as the unidentified infrared emission bands or UIBs, were first identified as due to polycyclic aromatic hydrocarbons (PAHs) by Léger & Puget (1984). Since that time, our understanding of these features has become rather sophisticated, as more and more observational constraints have been produced, principally by the *ISO* mission (Peeters 2002). At the time of writing, the *Spitzer Space Telescope* is providing stunning new images in the PAH bands. Clearly, any serious attempt to model SEDs must now include a good deal of PAH physics, and in the following subsections we describe the treatment of PAHs within the mappings code.

In modeling the PAHs within photoionized regions we have opted for simplicity over an exact treatment, especially as the constraints on both the physics and the species of PAHs remain so poor. In the MAPPINGS IIIq code we have simply assumed that all the PAHs can be represented by a single representative type, coronene ($C_{24}H_{12}$). Not only has coronene been observed within the ISM, but it is also pericondensed, reasonably stable, and can adequately match the observational constraints in the UV and IR. Although perhaps slightly smaller than the average ISM PAH (Allamandola et al. 1999), it has the great advantage that there exists a large amount of laboratory data for it, and hence any modeling done with these data can be considered reasonably accurate from a purely physical viewpoint.

The spectroscopic properties (emission and absorption) of a PAH molecule depends on the number of carbon atoms (N_C), the hydrogenation (H per C), and the charge state of the molecule. In addition to these, the optical properties are affected by the shape of the PAH (cata- or peri-condensed) and the addition of end groups (like methyl-CH_3). In the modeling, we assume a pericondensed structure with no additional end groups. The PAH abundance within the code is determined by the amount of carbon depleted onto PAH molecules. This was chosen to provide a good match to the absolute strength of the PAH emission features in the infrared.

The use of a single species of PAH makes the determination of PAH survival, optical properties, and charge much easier to determine. The absorption, emission, and photoelectric processes on a single size and shape are also much more readily calculated. Li & Draine (2001), using all this available data, have constructed absorption cross sections for both neutral and ionized "astronomical" PAHs from the FUV to FIR. They did this for a range in N_C, with the largest of PAHs blended in with the optical properties of graphite grains.

Within MAPPINGS IIIq, we have used their data[1] to represent the PAH optical properties. The PAH optical data of Li & Draine (2001) is defined in terms of a PAH "radius," such that there is a continuum in data between PAH and graphite grains. This PAH radius connects directly with N_C, with $a = 10(N_C/468)^{1/3}$ Å. This gives for coronene an effective radius of $a = 3.7$ Å and surface area of 173 Å^2. These values, and the corresponding Li & Draine (2001) data for this size, are used within the code to define the effective PAH molecule. We use both the neutral and ionized PAH optical data for the code. The fraction contributed to the total PAH opacity is determined by the charge state of the model PAH, which is determined by the balance of electron sticking and photoelectric ejection.

4.2. *The PAH Emission Spectrum*

The emission spectrum of PAHs is determined by the natural modes of vibration, bending, and other deformation of the carbon skeleton, modified by the effect of the dangling groups and the electric charge state of the molecule. The principal modes and their characteristic wavelengths are:

3.29 μm Aromatic C−H stretch ($v = 1$–0);
3.40 μm Aliphatic C−H stretch (the $v = 1$–0 antisymmetric mode);
3.51 μm Aliphatic C−H stretch (the $v = 1$–0 symmetric mode);
6.2 μm and 7.7–7.9 μm C−C skeletal deformations;
8.6 μm C−H in-plane bend;
11.2 μm C−H out-of-plane bend (solo mode);
11.9 μm C−H out-of-plane bend (duo mode);
12.7 μm C−H out-of-plane bend (tri mode); and
15–20 μm C−C−C bending modes (Van Kerckhoven et al. 2000).

These emission features can be adequately represented by Lorentzian fits (Boulanger et al. 1998) of the form

$$F(x) = \frac{(A/\pi\sigma)}{\left[1 + (x - x_0)^2/\sigma^2\right]}, \tag{14}$$

in which $x = 1/\lambda$ cm^{-1}, the central wavenumber of the feature is x_0, the FWHM $= 2\ \sigma$, and the area under the curve is A.

Two model fits were made, the first to the data of Boulanger et al. (1998) for the ρ Ophiuchus dark cloud and for NGC 7023, and the second to the data of Laurent et al. (2000) for the M82 starburst. The second fit used more components, as listed in Verstraete et al. (2001), and also included a two-component fit to the 15–20 μm C−C−C bending modes (Van Kerckhoven et al. 2000). This fit applies to the Orion Bar region, M17 SW, and NGC 2023. The final model PAH emission spectrum adopted for the MAPPINGS IIIq code is given in Table 1.

Emission within the MAPPINGS IIIq code is treated as an energy conservation process. In equilibrium all the energy gained by a PAH through the absorption of photons can be lost through either photoelectric processes or IR emission. The fraction of the energy lost through photoelectric processes is determined, and we assume that the remaining fraction of energy is reemitted in the IR according to our empirical fit to the astrophysical PAH emission bands (UIBs).

This is not an exact treatment, as the PAH molecules will likely undergo stochastic heating processes and will lose some of their energy through IR continuum emission instead of via these fluorescent bands. However, the code also allows for very small graphite grains, which do undergo stochastic heating; thus both forms of emission are catered for.

TABLE 1
Fit to PAH Emission Components

λ (μm)	x_0	Peak	σ
3.39	3040.3	1.049E−4	20.40
6.2 (Component 1)	1608.5	4.738E−4	31.62
6.2 (Component 2)	1608.5	6.768E−4	12.1
6.2 (Component 3)	1593.9	3.113E−4	34.90
6.949	1440	3.214E−4	100
7.5	1328.5	6.768E−4	44.72
7.6	1311.3	9.730E−4	14.0
7.8	1274.3	1.438E−3	35.0
8.6	1163.1	1.015E−3	30.0
10.0	998	2.115E−4	158
11.3 (Component 1)	889.4	1.015E−3	8.8
11.3 (Component 2)	889.8	2.200E−3	5.68
11.3 (Component 3)	880.9	1.354E−3	15
12.7	787	1.015E−3	30.1
13.6	735	1.184E−4	14.9
14.3	699	1.099E−4	14.9
16.4	610	4.230E−4	17
17.8	562	2.961E−4	30.0

4.3. *PAH Photodestruction*

Where detailed measurements have been made of the distribution of PAH emission within compact H II regions, it is found that the PAH avoids the ionized regions, and is instead found in a narrow zone of emission (the photodissociation region) beyond the outer boundary of the ionized gas (Burton et al. 2000). This is clear evidence that PAH molecules cannot survive for significant lengths of time in the hostile environment in the ionized zones of an H II region. This is to be expected, because the photodissociation timescales in this region are very short. However, PAHs can survive, and are excited into emission in the photodissociation regions (PDRs) outside the ionized H II region.

The condition for photodestruction can be set in a number of ways. The simplest is that the presence of hard photons leads to rapid photodissociation in the ionized gas. In this case, the PAHs are destroyed in the ionized gas, and their C is returned to the gas phase.

A somewhat more sophisticated approach would be to say that PAHs are destroyed whenever the absorption-weighted mean radiation field (not necessarily ionizing) results in a photodissociation timescale that is short compared to the residence time of the PAHs in that radiation field. In this case we would compare photodissociation timescales with dynamical timescales to obtain a criterion for survival.

A still more sophisticated approach posits the possibility that photodissociation (by the ejection of an acetyleneic group) is countered by repair through accretion of carbon atoms (Allain et al. 1996a, 1996b). In this case, if $\tau_{\rm diss}$ is the radiative dissociation timescale and $\tau_{\rm acc}$ is the C atom accretion timescale, then

$$\tau_{\rm diss} = (F_{\rm FUV}\sigma_{\rm diss})^{-1}, \tag{15}$$

$$\tau_{\rm acc} = (n_{\rm H}X_{\rm C}k_{\rm acc})^{-1}, \tag{16}$$

[1] Available at http://www.astro.princeton.edu/~draine/dust/dust.diel.html.

where $F_{\rm FUV}$ is the FUV radiation field, $\sigma_{\rm diss}$ is the effective photodissociation cross section per PAH molecule for this particular radiation field spectrum, $n_{\rm H}$ is the number density of hydrogen atoms, $X_{\rm C}$ is the abundance of C in the ISM, and $k_{\rm acc}$ is the reaction rate for sticking of a carbon atom onto such a molecule. For the FUV radiation field, we take the total radiation field above the ionization potential adopted for these molecules ($\geq$6 eV). This provides the condition for PAH destruction (Dopita et al. 2002b):

$$F_{\rm FUV}\sigma_{\rm diss} > n_{\rm H}X_{\rm C}k_{\rm acc},$$

or

$$\mathcal{H} = \frac{F_{\rm FUV}}{cn_{\rm H}} > \frac{X_{\rm C}k_{\rm acc}}{\sigma_{\rm diss}}, \qquad (17)$$

where $\mathcal{H}$ is the Habing photodissociation parameter, defined by analogy with the dimensionless ionization parameter $\mathcal{U}$ used in H II region theory. From observation, values of $\mathcal{H} \sim 0.05$ are observed in regions that still contain PAHs (Allain et al. 1996a). However, this is a line-of-sight average, which provides only an upper limit. A threshold of $\mathcal{H} \sim 0.005$ for the destruction of PAHs ensures that PAHs are excluded from the H II regions, but are present in the PDRs of even the compact H II regions. However, similar results are obtained by assuming that PAHs are destroyed on a short timescale whenever the spectrum-averaged photodissociating field exceeds about 10 times the local interstellar field. Both of these formulations are available within the MAPPINGS IIIq code. In this paper we have opted to use the Habing photodissociation parameter formulation with $\mathcal{H} \sim 0.005$, which effectively excludes PAH from surviving within the ionized gas.

When the threshold of $\mathcal{H} \sim 0.005$ is exceeded locally, we have assumed that the PAHs are destroyed in our models, and in this case we return the carbon that they contain to the gas phase. In starburst galaxies, this condition is sufficient to ensure that the PAHs are destroyed in both the ionized and in the warm diffuse media. Since the PAH absorption cross section is like that of carbonaceous grains, this means that most of the carriers of the 2200 Å absorption are removed from lines of sight that permit the UV stellar continuum to escape. As we show below, this provides a natural explanation of why the 2200 Å feature is weak or absent in the UV spectra of active galactic nucleus (AGN) or starburst galaxies (Calzetti 2001), provided that small organic grains or other carbonaceous types are not present in high abundance.

5. GRAIN SIZE DISTRIBUTION AND COMPOSITION

The grain size distribution and the grain composition are the principal factors that determine the wavelength dependence of the absorption and scattering processes. The grain size distribution in the ISM results from the balance between the grain formation and destruction processes. It varies as a power law over a wide range of sizes, a (Mathis et al. 1977, hereafter MRN):

$$dN(a)/da = ka^{-\alpha}, \quad a_{\rm min} \leq a \leq a_{\rm max}, \qquad (18)$$

where α, $a_{\rm min}$, and $a_{\rm max}$ are derived by an empirical fit to the scattering and extinction in the local ISM. For the MRN distribution, the minimum size is set to $a_{\rm min} = 0.005$ μm for carbonaceous grains, and to $a_{\rm min} = 0.01$ μm for silicaceous grains. For both grain types, $a_{\rm max} = 0.25$ μm.

A more complex distribution has been suggested on physical grounds (Weingartner & Draine 2001), and this takes into account both silicate and carbon-containing grains with different grain size distributions. For the carbonaceous grains, the PAHs are treated as providing an additional component on a continuous distribution of grain sizes. Even these distributions can be approximated by power laws over a wide range of radii.

Grain shattering has been shown to lead naturally to the formation of a power-law size distribution of grains with $\alpha \sim 3.3$ (Jones et al. 1996), observationally indistinguishable from the MRN value, $\alpha \sim 3.5$. Such a grain size distribution can also hold only between certain limits in size, the smaller size being determined by natural destruction processes such as photodestruction, and the upper limit being determined by limits on the growth by condensation and sticking. To capture these elements of the physics, we have adopted a modified grain shattering profile with the form

$$dN(a)/da = ka^{\alpha}\,\frac{e^{-(a/a_{\rm min})^{-3}}}{1 + e^{(a/a_{\rm max})^{3}}}. \qquad (19)$$

This creates a smooth exponential cutoff in terms of the grain mass at both the minimum and maximum grain size of the distribution. This smooth cut removes any edge effects in either the emission or extinction by dust that arise because of the sharp cutoffs in the other distributions. Our distribution does not have the extra bump to accommodate the PAHs, since they are treated as a separate molecular component, as described above.

The grain size limits for both graphitic and silicaceous grains are set to $a_{\rm min} = 0.004$ μm and $a_{\rm max} = 0.25$ μm. The somewhat smaller size cutoff than the MRN distribution provides a stronger dust re-emission continuum below 25 μm, which is needed to fit the observed *IRAS* colors of starbursts (Rush et al. 1993). The constant k is determined by the total dust-to-gas mass ratio, which is determined by the depletion of the heavy elements onto dust. Our models use a solar abundance set (as modified by the latest abundance determinations Allende Prieto et al. 2001, 2002; Asplund 2000; and Asplund et al. 2000; see Table 2). The depletion factors are those used by Dopita et al. (2000) for starburst and active galaxy photoionization modeling and are similar to those found by Jenkins et al. (1983) and Savage & Sembach (1996) in the local ISM using the UV absorption lines to probe various local lines of sight.

Within the MAPPINGS IIIq code, the dust grain size distribution is divided into 80 bins spaced logarithmically between 0.001 and 10 μm. The number of grains of each type in each bin is then determined by equation (19). The absorption, scattering, and photoelectric heating is calculated for each size bin. This is then used to establish the temperature probability distribution for computation of the FIR re-emission spectrum with quantum fluctuations.

When present, the PAHs are set at an abundance which uses 110 ppm of carbon. Consequently, the carbonaceous grain component is present at only rather low abundance; equivalent to 69 ppm of carbon.

5.1. *Grain Quantum Fluctuations*

In order to properly model the FIR emission bump, it is very important to take stochastic quantum heating of the dust grains into account. In particular, the temperature fluctuations of grains serves to provide a population of small grains that are hotter than their equilibrium temperature and thus have an excess in their IR emission at shorter wavelengths.

TABLE 2
Solar Abundance Set ($Z_\odot$) and Logarithmic Depletion Factors Adopted for Each Element

Element	log ($Z_\odot$)	log D
H	0.00	0.00
He	−1.01	0.00
C	−3.59	−0.52
N	−4.20	−0.22
O	−3.34	−0.22
Ne	−3.91	0.00
Na	−5.75	−0.60
Mg	−4.42	−0.70
Al	−5.61	−1.70
Si	−4.49	−1.00
S	−4.79	−0.22
Cl	−6.40	−0.30
Ar	−5.44	0.00
Ca	−5.64	−2.52
Fe	−4.55	−2.00
Ni	−5.68	−1.40

This idea of the temperature fluctuations in small grains can be extended to the very small grains or molecules, such as PAHs. These are much more likely to undergo such a fluctuation, although the possibility of destruction by a singe photon is also increased. The point at which a dust grain, which cools through a continuous radiative decay, should be considered as a dust molecule, which "cools" (enters lower vibrational states) through discrete vibrational and rotational quantum states, is rather ill-defined. Here we have taken the simple approach and treated all dust as grains having well-defined bulk properties, with the molecular treatment being reserved for the PAH population.

Temperature fluctuations and stochastic heating processes have been considered by several authors since Greenberg first suggested these ideas (e.g., Duley 1973; Greenberg & Hong 1974; Purcell 1976; Dwek 1986). The most detailed work on dust and temperature fluctuations has been a series of papers by Draine and coworkers (Draine & Anderson 1985; Guhathakurta & Draine 1989), culminating in a set of papers with Li (Draine & Li 2001; Li & Draine 2001).

The FIR emission treatment used in the MAPPINGS IIIq code, whose results are presented here, is based on the algorithms of Guhathakurta & Draine (1989) and Draine & Li (2001). The code provides an optimized solution of their algorithms to determine the dust grain temperature distributions for each grain size according to the both the strength and the detailed spectrum of the local radiation field. The code then integrates the resulting FIR emission of the ensemble of dust grains to provide the local re-emission spectrum, which is itself integrated through the model in the outward-only approximation.

6. ATTENUATION BY DUST: IR TO UV

If our dust model is really representative of the dust found in starburst galaxies, then it should reproduce the wavelength-dependent attenuation law seen in starburst galaxies (Calzetti 2001). Here we use the word "attenuation" to distinguish it from extinction, since it properly describes the wavelength-dependent escape fraction of starlight from the galaxy averaged across all possible sight lines rather than the wavelength dependence of the effective extinction optical depth along a single sight line.

Models of the attenuation show that it can be well represented by the effect of a foreground screen (Meurer et al. 1997, 1999). In an earlier paper, Fischera et al. (2003) showed that many features of the Calzetti attenuation law for starbursts (Calzetti 2001) could be reproduced by turbulent screen having a lognormal column density distribution. The grain model used in that paper was that of Weingartner & Draine (2001), which, being strictly applicable to the local ISM, gave a strong 2200 Å

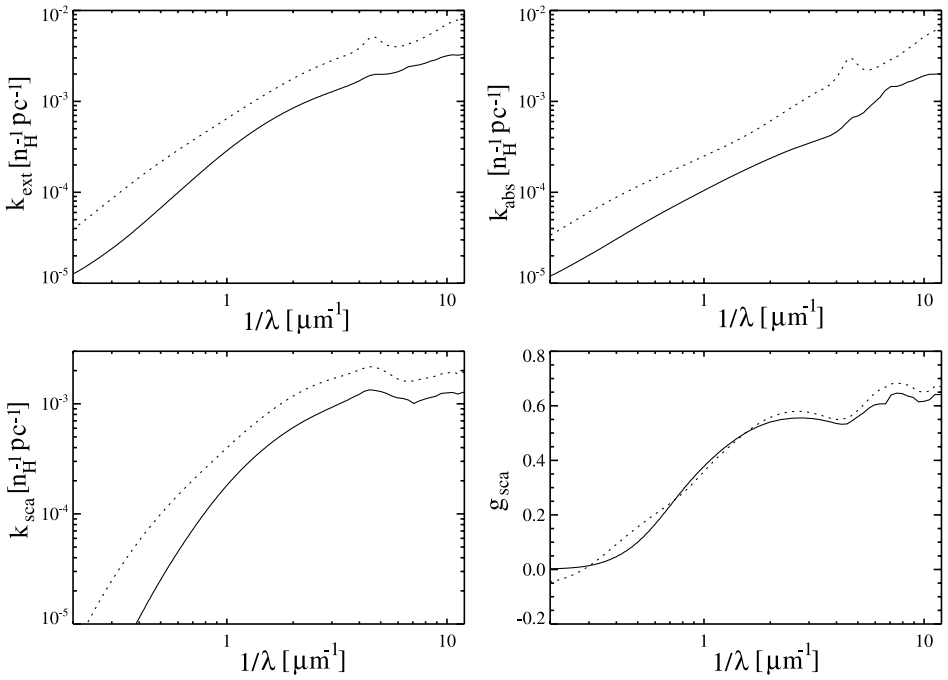

Fig. 3.—Extinction, absorption, scattering, and g-factor (*thick solid lines*) of our dust model for the diffuse phase of the ISM in which the UV field is sufficiently strong for PAHs to be destroyed. This component is assumed to provide the foreground screen attenuation for the starburst. The absolute to relative extinction is $R_V = 3.38$. The dotted curves show the corresponding values for the local interstellar medium of our galaxy as defined by Weingartner & Draine (2001). The generally lower opacity of our grain model mostly reflects the lower abundances associated with the revised solar abundance set.

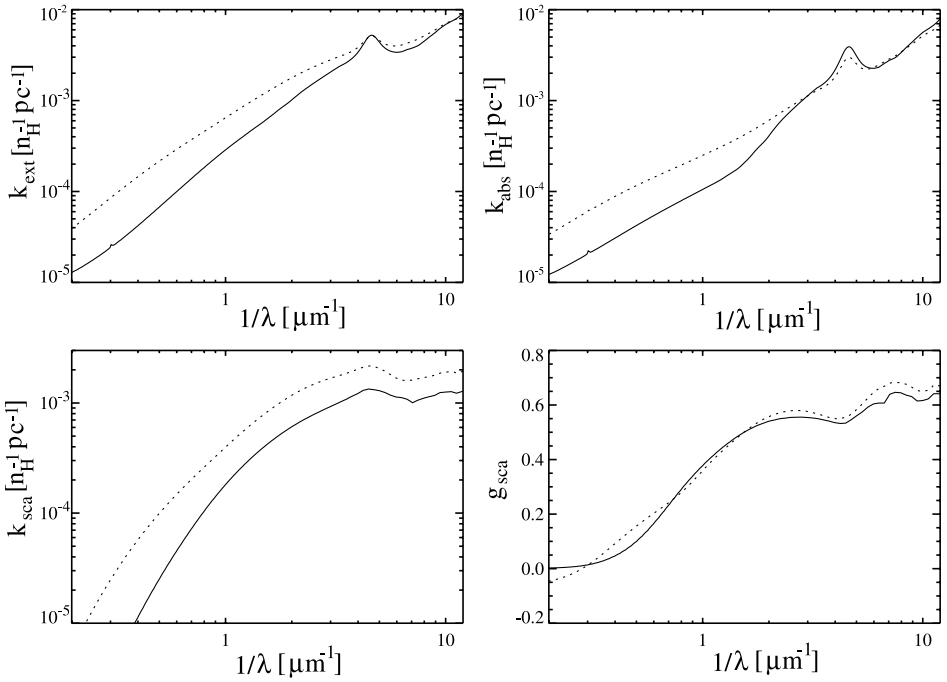

FIG. 4.—Extinction, absorption, scattering, and g-factor for our dust model in which 110 ppm of the carbon is assumed to be condensed in PAH. Solid curves correspond to our assumed grain and PAH populations in the PDRs and molecular clouds. Note the extreme strength of the 2200 Å absorption, and the deficit in the absorption and extinction at IR wavelengths, relative to the Weingartner & Draine (2001) grain model (*dashed curves*). For this grain model the absolute to relative extinction is $R_V = 1.92$.

absorption feature. However, this feature is not evident in the attenuation curves of either starburst galaxies or AGNs.

Here we formulate the hypothesis that the major carrier of the 2200 Å absorption feature are the PAHs, which are, as we have seen, effectively destroyed within the strong UV radiation field environments of the diffuse neutral or ionized phases of the ISM. They do, however, persist in the PDRs around the boundaries of dense molecular clouds, where they are strongly excited to fluoresce in the "UIB" PAH features in the infrared. These molecular clouds are completely opaque to the passage of optical and UV photons, and so provide only a geometrical covering factor to the attenuation at these wavelengths.

This model offers the potential both to explain the absence of the 2200 Å absorption feature *and* the great intensity of the UIBs in starburst galaxies. Does it work?

In Figure 3, we show the wavelength dependence of the optical properties of our dust model compared with that of Weingartner & Draine (2001). It is clearly apparent that the 2200 Å absorption feature is strongly suppressed by our grain model, but otherwise that the extinction and scattering properties of our grain mix is quite similar to the Weingartner & Draine (2001) results once the offset due to the abundance set is accounted for.

For comparison, we show the optical data for our grain model for the PDRs. Here the 2200 Å feature is very strong, and the IR opacity low. A linear combination of the model curves in Figures 3 and 4 would produce an outcome that is almost indistinguishable from those of Weingartner & Draine (2001).

We have used the optical parameters of Figure 3 to construct an extinction curve for this grain model. This is shown as the thin solid line on Figure 5. We then used the same procedure as described in Fischera et al. (2003) to derive an attenuation curve appropriate to a turbulent foreground screen having a lognormal distribution in column densities and having an R_V value of 4.0, consistent with that obtained for the Calzetti curve ($R_V = 4.04$). Our theoretical attenuation curve is shown on Figure 5 as the thick solid line, for comparison with the Calzetti empirical attenuation curve for starbursts (*dashed line*).

It is clear that our grain model is extremely successful in reproducing the Calzetti empirical law to an accuracy that lies within the observational errors in the empirical fit. This success relies both on the destruction of the PAHs in the diffuse phases of the ISM, and on the low abundance of other carbonaceous grain types, which was forced upon us by the need to satisfy C abundance constraints while at the same time ensuring that the strength of the PAH emission bands matched observational constraints.

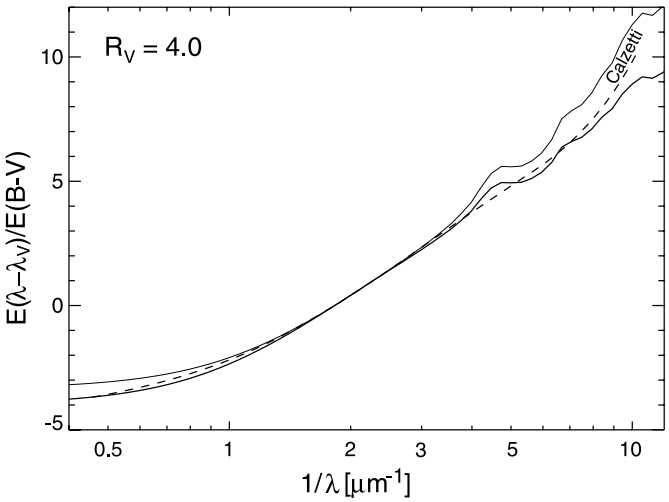

FIG. 5.—Attenuation curve for a turbulent dusty foreground screen (*thick solid line*) derived using our dust model. The R_V value is chosen to be 4.0, consistent with the value of the Calzetti curve ($R_V = 4.04$). The Calzetti attenuation curve is shown as dashed line and is identified by name. The initial extinction curve for our dust model is shown as thin solid line.

TABLE 3
RELATIVE ATTENUATION $E(\lambda - V)/E(B - V)$, FOR $R_V = 4.0$ ($A_V = 1$)

λ (μm)	Waveband or Feature	This Work	Calzetti (2001)	Weingartner & Draine (2001)
0.0912	Ly∞	9.164	11.033	8.591
0.1053	...	8.542	9.198	7.308
0.1216	Lyα	7.397	7.765	5.885
0.1550	C IV	5.999	6.062	4.310
0.1906	C III]	4.954	5.037	4.471
0.2175	2175	4.839	4.415	5.619
0.2480	...	3.904	3.790	4.025
0.3000	...	2.759	2.862	2.729
0.3650	U	1.839	1.896	1.847
0.440	B	1.000	1.000	1.000
0.458	V	0.000	0.000	0.000
0.720	R	−1.177	−1.111	−1.103
1.030	I	−2.432	−2.267	−2.211
1.239	J	−2.905	−2.720	−2.626
1.649	H	−3.401	−3.275	−3.105
2.192	K	−3.682	−3.690	−3.444

For the convenience of observers, we give this theoretical attenuation law in tabular form in Table 3. Data values are given in terms of the variable

$$\xi_\lambda = \frac{A_\lambda - A_V}{A_B - A_V} = \frac{E(\lambda - V)}{E(B - V)}, \tag{20}$$

and the absolute attenuation can be calculated from these values by

$$A_\lambda = (\xi_\lambda / R_V + 1) A_V \tag{21}$$

with $R_V = 4.0$.

7. MODELING THE STARBURST

We assume that the starburst region occupies a roughly spherical region filled with H II regions of all possible ages; the exact shape of the starburst region does not alter the results of the modeling. At any age, these H II regions have a radius determined by both their age and the pressure in the ISM, according to Figures 1 and 2. The region around the starburst is assumed to be filled with a warm, dusty PAH-free diffuse ISM, which provides a foreground screen extinction as described in § 6. The starburst is assumed to form stars at a rate of 1 $M_\odot$ yr^{-1} for a total period of 10^8 yr, and since each cluster has 10^4 $M_\odot$ of young stars, there are 1000 H II regions younger than 10 Myr. After 10 Myr, the ionizing photon output of the central cluster has dropped to negligible levels. Stars older than 10 Myr are distributed within the H II regions in proportion to the volumes of the individual H II regions. The H II regions are assumed not to be "leaky" to the EUV photons. That is to say, they fill their Strömgren spheres and so absorb all the ionizing photons.

The input stellar spectra (stellar cluster+old stars) within the volume of an H II region of given age are computed using the STARBURST99 code as described above. The MAPPINGS IIIq code is used with these stellar spectra to compute the radiative transfer through the ionized gas, the equilibrium ionization and temperature, and the dust and nebular line and continuum spectra throughout the individual H II regions. The MAPPINGS IIIq models have an isobaric density structure, where the internal pressure is defined by our evolutionary modeling (see Fig. 2), and their physical size matches the computed diameter (see Fig. 1). The integrated output spectra are weighted by the number of H II regions in each time step, to give the flux equivalent to a galactic mean star formation rate of 1 $M_\odot$ yr^{-1}. The time sampling of the individual models is first at 0.4 Myr, then at 1 Myr, and then at 1 Myr age intervals up to 10 Myr.

We should note here that the MAPPINGS IIIq code treats the radiative transfer in the outward-only approximation, scattered photons being divided into an outward stream and a backscattered stream, which is assumed to return across the ionized nebula.

Following Silva et al. (1998) and Popescu et al. (2000), we consider each H II region to be surrounded by an incomplete opaque shell of molecular gas, in pressure equilibrium with the ionized plasma, which blocks a fraction of the incident stellar light according to the geometrical covering factor. The PDR at the inner boundary of the molecular shell absorbs almost all of the incident FUV, UV, and optical photons. To ensure that this is the case, the models were continued into the PDR until an H I column of $\log n_{\rm HI} = 21.5$ was reached. This corresponds to $A_V \sim 3$ mag, equivalent to nearly 10 mag at the Lyman limit. Thus, effectively all the stellar photons and photons of nebular origin that can excite the PAHs, or produce FIR continuum shortward of 100 μm, are fully absorbed in the PDR.

If the incomplete shell covers a fraction $f = \Omega/4\pi$ of the total solid angle, then in the remaining $1 - f$ of the solid angle, both the remaining (unabsorbed) stellar photons and the photons produced in the H II region are assumed to escape from the starburst region. Some of these will be lost in the outer foreground turbulent dusty screen, but the additional attenuation produced here can be calculated using the results of § 6. The factor $1 - f$ is therefore the escape probability for the stellar photons which successfully exit the starburst region. In this sense, the molecular clouds serve to provide a "gray" attenuation factor of $1 - f$.

Since the hot stars are born in molecular clouds, and these clouds are dissipated during the lifetime of the H II region as the region evolves from compact to classical shell morphology, it is clear that the molecular cloud covering factor f is a decreasing function of time. This concept of age-selective obscuration was first introduced by Silva et al. (1998), and was employed by Tuffs et al. (2004) in their calculation of the attenuation of starlight in normal galaxies. Here we investigate two cases. In

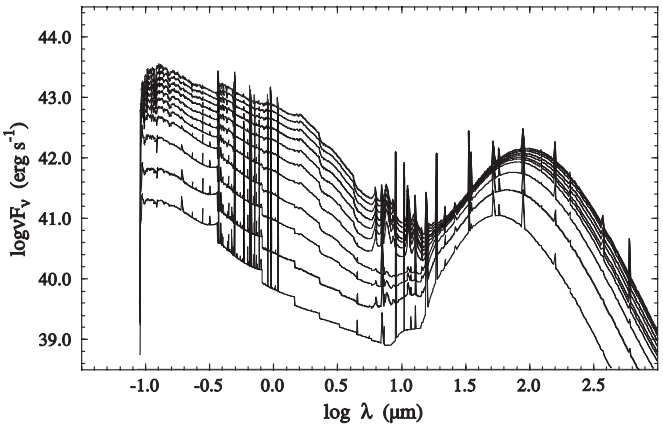

FIG. 6.—Cumulative SED for the H II regions and their stars of different ages, 0.4 (*lower curves*) to 10 Myr (*top*). The older stars are included within the volume of the H II regions. Each contributing spectrum is weighted in proportion to its covering factor, $1 - f(t)$. The case in which the covering factor decreases linearly with time and the ISM pressure $P/k = 10^4$ cm^{-3} K is shown here (see text). [*See the electronic edition of the Journal for a color version of this figure*.]

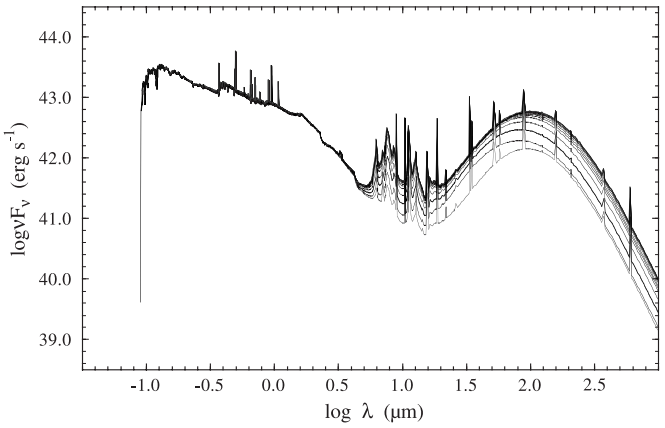

FIG. 7.—Cumulative SED of Fig. 6 (*bottom curve*), to which has been added the contributions of the optically thick portions of the H II regions and their PDRs with ages from 0.4 (*lower curves*) to 10 Myr (*top curve*). As in Fig. 6, the case of the ISM pressure $P/k = 10^4$ cm^{-3} K is shown, and the case for which the covering factor changes linearly with time (see text). Each contributing spectrum is added with a weight in proportion to its covering factor $f(t)$. [*See the electronic edition of the Journal for a color version of this figure*.]

the first, the covering factor decreases linearly with time from 0.9 at 1 Myr to 0.1 at 9 Myr, is complete at 0 Myr and equal to 0.1 at times later than 9 Myr. Since this function is a little arbitrary, we also investigate the more general case in which the covering factor decreases exponentially with time,

$$f(t) = \exp(-t/\tau_{\rm clear}) \qquad (22)$$

with the molecular cloud clearing timescale, $\tau_{\rm clear}$, set to 1, 2, 4, 8, 16, and 32 Myr. It turns out that the linear case provides an SED that is indistinguishable from the exponential case and has an effective timescale $\tau \sim 7$ Myr.

Since, in general, there will be no physically a priori way of constraining the molecular cloud clearing timescale, we are forced to leave it as a free parameter, which we hope can be constrained by the observed SED or colors of real starburst regions.

To show the way in which the final SEDs are composed of the sums of many H II region models, and to demonstrate that all models provide important contributions to the final SED, we display the cumulative SEDs resulting from this addition for H II regions of ages 0.4–10 Myr in Figures 6 and 7. These figures apply to the case in which the molecular cloud covering factor decreases linearly with time, and for an ISM pressure $P/k = 10^4$ cm^{-3} K. The y-axis is chosen to display the energy flux νF_ν, rather than F_ν, in order to better show how the FIR bump redistributes the UV stellar continuum. The absolute scale for the summed SED corresponds to the star formation rate of 1.0 $M_\odot$ yr^{-1} used in the models.

In Figure 6, which shows the fraction of flux escaping from the H II regions, note the strength of the nebular lines and continuum, the weakness or absence of PAH features, the hot dust temperatures, and the presence of silicate absorption in the infrared spectra of the youngest H II region models. For these models, the stellar continuum dominates only in the UV. In the visible and near-IR the nebular continuum dominates, with the bound-free edges prominent.

After about 3 Myr, the red supergiant stars appear, with their characteristic CO features in the H and K bands. For these models of older clusters, the stellar continuum dominates the SED up to about 5 μm.

In Figure 7, the additional contribution to the SED by the H II region in the remaining solid angle and by the photodissociation regions is shown. In these spectra, all the stellar the UV continuum radiation has been absorbed in the PDR and converted to dust re-emission, which thanks to the low optical depth in the IR is free to escape. Note how the peak of the FIR dust re-emission bump shifts to longer wavelengths for the models with the older central clusters. This is a consequence of both the decrease in the stellar luminosity and the larger shell sizes, which both lead to lower dust temperatures. In addition, the PAH emission bands are stronger in the older H II regions. In these models, the PAHs survive thanks to the lower photodestruction rates of the PAHs resulting from the lower UV fluxes and cooler stellar temperatures. Nonetheless, there are still plenty of photons with $6 \leq h\nu \leq 13.6$ eV to be absorbed by the PAHs and to excite the UIB features.

Thus, our models can succeed in explaining the apparently contradictory observations that starburst galaxies are seen to have very strong UIB emission (implying the presence of large quantities of photoexcited PAH molecules), but have no sign of the UV 2200 Å absorption feature (implying the absence of PAHs, or at least carbonaceous grains, in the more diffuse phases of the ISM).

8. PARAMETERS CONTROLLING THE SED

In this section, we present the results of the systematic investigation of the two parameters which, apart from the optical depth of the foreground absorbing screen, the assumed dust grain size distribution, and the assumed dust composition, primarily control the SED of the starburst. These parameters are identified as the mean pressure in the ISM and the molecular cloud covering factor.

8.1. *The Role of Pressure*

We have computed three sets of models with different pressures, $P/k = 10^4$, 10^6, and 10^7 cm^{-3} K. The first of these corresponds roughly to the pressure in the ISM near our Sun (Jenkins 1983), and so would be applicable to star formation complexes in disk galaxies.

Pressures of $P/k \sim 10^6$ are commonly encountered in starburst galaxies, and can be measured using either the emission

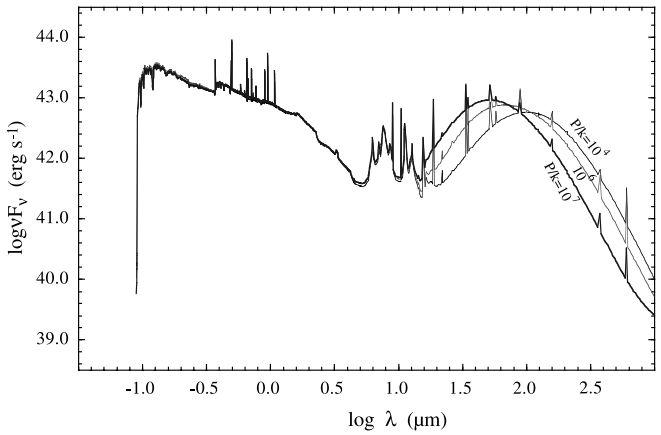

FIG. 8.—Summed starburst SEDs computed for ISM pressures $P/k = 10^4$, 10^6, and 10^7 cm^{-3} K, for the case in which the molecular cloud covering factor changes linearly with time. [*See the electronic edition of the Journal for a color version of this figure.*]

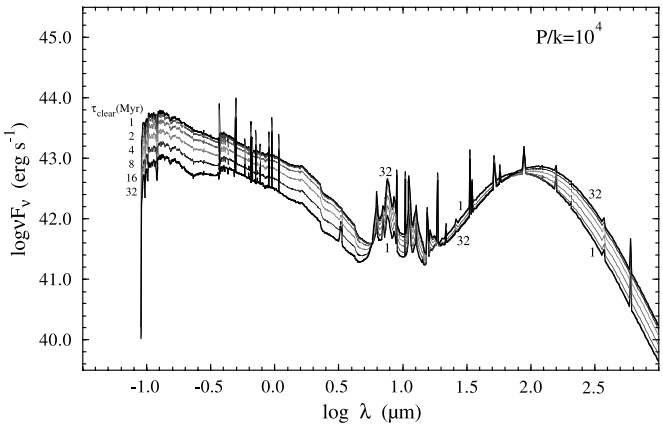

FIG. 9.—Summed starburst SEDs computed for ISM pressure $P/k = 10^4$ cm^{-3} K, with exponential molecular cloud clearing timescales of 1, 2, 4, 8, 16, and 32 Myr. Note that a long clearing timescale depresses the UV continuum but leads to stronger PAH emission as well as stronger ~100 μm dust emission. [*See the electronic edition of the Journal for a color version of this figure.*]

measure in the H II regions or even using the density-sensitive [S II] $\lambda\lambda$6717/6731 ratio, provided that $n_e \geq 100$ cm^{-3}. Starbursts with these pressures are characterized by warmer *IRAS* colors (Kewley et al. 2001a, 2001b).

Finally, starbursts with $P/k \sim 10^7$ have the warmest *IRAS* colors, and are most often the nuclear starbursts in postmerger galaxies. For these, the [S II] $\lambda\lambda$6717/6731 ratio indicates $n_e \geq$ 1000 cm^{-3} (Kewley et al. 2001a, 2001b). Thus, our choice of parameters should cover the full range seen in real starburst galaxies.

Figure 8 shows the effect of the changing pressure on the SEDs. The main change is the progressive shift of the peak of the FIR dust re-emission bump to shorter wavelengths, and the increase in its flux. For a pressure of $P/k = 10^4$ the peak is at 105 μm, at $P/k = 10^5$ the peak is at 70 μm, and by $P/k = 10^7$ the peak has shifted down to 50 μm. At this high pressure, hot dust emission can be traced to as wavelengths as short as 4 μm.

For all these curves, there is no discernible change in the stellar continuum. This is to be expected, as it is defined by the geometrical constraints. However, there is a progressive change in the nebular line spectrum toward higher excitation at higher pressure. This is a consequence of the mean ionization parameter, which slowly increases as the pressure increases.

Surprisingly enough, the strength of the PAH emission features is almost invariant with pressure. This is because the PAH molecules can survive in the PDRs independently of the pressure, since the photodissociation rates are low in these zones. Thus, the PAH features scale only with the covering factor, *f*.

We would expect these theoretical SEDs to be not very accurate at wavelengths above 100 μm because we have not taken into account the dust re-emission either of diffuse starlight, or caused by stars older than 10^8 yr. Nor have we included the FIR re-emission by foreground dust outside the main star-forming region. Thus, we would expect that in real starburst galaxies there will be a cold component of dust emission from the ambient medium that is not predicted by this model. However, for starburst galaxies the results in § 9 show the fit to be remarkably good. Nonetheless, the absence of this component will certainly become a serious problem for the modeling of "normal" (nonstarburst) galaxies, since we know that for these galaxies the luminosity of the cold dust component generally exceeds that of the locally heated dust (e.g., Popescu et al. 2002). High-resolution maps of galaxies like M31 (Haas et al. 1998), M33 (Hippelein et al. 2003), or NGC 891 (Popescu et al. 2004) made in the *ISO* 170 or 200 μm bands all show that most of this cold dust luminosity is carried by the diffuse ISM, not by the optically thick molecular clouds. Thus, the model presented in this paper is not really applicable to normal galaxies. For this, the output SED of the H II regions computed here will have to be incorporated in a model such as that of Popescu et al. (2000) that self-consistently calculates the radiation transfer in the diffuse component of the ISM.

Another way in which these theoretical SEDs may differ from those of real starburst galaxies is in the way collective effects may alter the form of the computed SED. In galaxies with a strong centrally concentrated starburst, H II regions may be superposed along the line of sight, and the radiative transfer would be then more complex than assumed in our model. Again, the solution to this is to build a three-dimensional radiative transfer model for the dusty gas, and to use the SEDs presented here as input source functions.

Finally, there may well be a population of dust-enshrouded and confined ultracompact H II regions contributing to hot dust emission. We might reasonably expect to find relatively more of these in high-pressure regions. In our own Galaxy the W3 complex provides precisely these conditions. At high pressure, the star-forming regions are embedded in denser molecular gas dust, and the H II regions stall sooner, and at smaller radii. Single OB stars would therefore find it difficult to blow their H II regions to sufficient size to be able to communicate with regions of lower density, and may therefore spend a significant part of their main-sequence lifetime in the compact or ultracompact H II region phases. We return to the evidence for such a population of compact H II regions in § 9.

8.2. *The Role of Covering Factor*

The molecular cloud covering factor has a significant effect on nearly all the starburst SED, as Figures 9, 10, and 11 make clear. These figures show the effect of the exponential molecular gas clearing timescale, $\tau_{\rm clear}$, at the three different pressures.

First, high covering factors lead to an attenuation of all the stellar continuum, which is dominant from the Lyman limit down to about 5 μm. However, when the molecular gas curtain is slow to open, there is a significant effect of aging in the stellar continuum, since the light from the oldest H II regions is dominant, and these H II regions, being largest, also contain the largest number of stars with ages above 10 Myr. This aging is

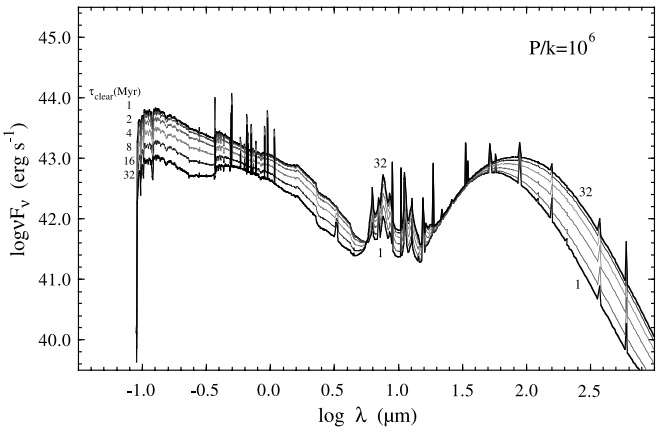

FIG. 10.—As in Fig. 9, but for $P/k = 10^6$ cm^{-3} K. Note the displacement of the FIR bump toward shorter wavelengths. [*See the electronic edition of the Journal for a color version of this figure.*]

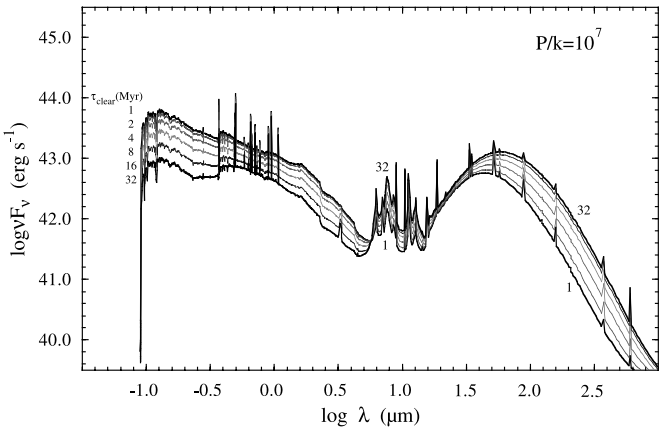

FIG. 11.—As in Fig. 9, but for $P/k = 10^7$ cm^{-3} K. [*See the electronic edition of the Journal for a color version of this figure.*]

visible as an increase in the size of the Balmer and Paschen discontinuities, and a flattening of the UV spectral slope.

Larger covering factors also lead to an increase in strength of the PAH features, and both a strengthening and broadening of the $\sim$100 μm dust emission peak. This strengthening of the peak works in the opposite direction from pressure, since the strengthening is due to an increasing contribution of the older H II regions with longer $\tau_{\rm clear}$. These older H II regions are larger, and consequently the dust in them is cooler.

At about 25 μm, the flux changes little with $\tau_{\rm clear}$ for all pressures. However, the flux at this wavelength is very strongly affected by affected by changes in pressures. By contrast, the stellar continuum and the PAH features are strongly affected by the molecular cloud covering factor, but changes in pressure do not affect these at all. This offers the potential to distinguish observationally between these two parameters, as we discuss below.

8.3. *Approximations to the Nonthermal Emission*

One of the results of our modeling is that the 60 μm flux depends quite strongly on the pressure in the interstellar medium. However, we also know from observation that there is an extraordinarily close correlation between the 60 μm infrared continuum and the radio 1.4 GHz continuum of star-forming galaxies. This linear correlation spans $\sim$5 decades of magnitude with less than 0.3 dex dispersion (Yun et al. 2001; Wunderlich et al. 1987), and the IR–radio correlation persists even when measurements of the cold dust emission (which carries the bulk of the FIR luminosity for normal galaxies) are included in the total FIR luminosity (Pierini et al. 2003). The mean relationship between the 60 μm flux and the 1.4 GHz continuum is

$$\frac{L_{1.4\ \rm GHz}}{\rm W\ Hz^{-1}} = 10^{12}\left(\frac{L_{60\ \mu\rm m}}{L_\odot}\right). \tag{23}$$

We know that, in star-forming galaxies at 1.4 GHz, the nonthermal emission by relativistic electrons dominates by at least an order of magnitude over the free-free emission (Condon 1992; Niklas et al. 1997; Dopita et al. 2002b). Therefore, and somewhat remarkably, this relationship couples a purely thermal process with a nonthermal process, over many decades of flux, and locally, within individual galaxies. Because of the intrinsic interest of this radio–FIR correlation, and because we have shown that ISM pressure directly affects one of the parameters that enters into this correlation, in this section we investigate a "toy" model of the synchrotron emission in order to gain insight into how the synchrotron emission might be similarly affected by the ISM pressure, thus keeping the radio–FIR correlation as tight as is observed.

If the lifetime of the synchrotron electrons is short compared with the evolution timescale of the starburst, then as Bressan et al. (2002) have shown, the synchrotron emissivity acts as a bolometer of the supernova rate, since the relativistic luminosity is ultimately derived from the Fermi acceleration process in supernova shocks. Specifically, the nonthermal luminosity is given by

$$L_{\rm NT}(\nu) \propto \dot{M}_* B^{\alpha-1}\nu^{-\alpha}, \tag{24}$$

where $\dot{M}_*$ is the total star formation rate. Since the observed spectral index lies in the range $0.5 > \alpha > 1.0$, there is only a very weak dependence on the magnetic field in this case.

If the lifetime of the relativistic electrons is long compared with the length of the starburst, then the emissivity of the relativistic electrons depends on the square of the local magnetic field, and on the local density of the relativistic electrons. Groves et al. (2003) ascribes the overall radio–FIR correlation, and its local variation in individual galaxies to the operation of magnetohydrodynamic turbulence.

In a magnetized and turbulent interstellar medium, numerical simulations (e.g., Cho & Vishniac 2000b) have shown that the local magnetic field will stay in equipartition with the gas turbulent energy,

$$\delta V \sim B/\sqrt{4\pi\overline{\rho}}. \tag{25}$$

This provides the coupling between the gas density and the magnetic field that is a necessary, but not a sufficient, condition for the operation of the radio–FIR correlation. This equation also ensures that the magnetic field pressure and the gas pressure are correlated.

The local synchrotron emissivity at frequency ν is given from the standard synchrotron theory by

$$j_\nu = f(a)kB^{(a+1)/2}\nu^{-(a-1)/2}, \tag{26}$$

where $f(a)$ is a complex numerical factor of a, the power-law slope of the nonthermal electron the number density of the relativistic electrons with relativistic γ, $N(\gamma)^{-a} = k\gamma^{-a}$, and B is the local magnetic field. The total density of the relativistic electrons is therefore $n_{\rm cr} = k\gamma_{\rm min}^{1-a}/(a-1)$, where $2 < a < 3$

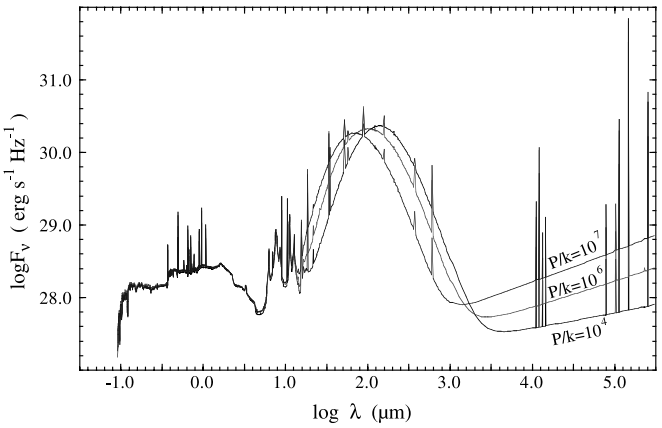

FIG. 12.—Summed SEDs (F_ν vs. λ) computed for ISM pressures $P/k = 10^4$, 10^6, and 10^7 cm^{-3} K for the case in which the molecular cloud covering factor changes linearly with time and for an absolute star formation rate of 1.0 $M_\odot$ yr^{-1}. Note that changes in the radio nonthermal luminosity with pressure are positively correlated with changes in the 60 μm flux. [*See the electronic edition of the Journal for a color version of this figure*.]

corresponds to a frequency spectral index of synchrotron emission $0.5 > \alpha > 1.0$. Provided that the relativistic electrons cannot escape from the star-forming region, the constant, k, should be proportional to the star formation rate. Equation (26) predicts, in contrast to equation (24), there should be a strong correlation between the emissivity and the magnetic field, in the range $B^{3/2}$ to B^2.

At normal ISM pressures, the lifetime of the relativistic electrons should be longer than the star formation timescale, so that equation (26) would apply. However, as the pressure increases, the emissivity of the nonthermal emission also increases, and the lifetime of the electrons becomes shorter. Thus, at high P/k, we expect that equation (26) ceases to apply, and we go over to equation (24) instead. Unfortunately, we have no way of estimating at which point this occurs with this simple theory.

In our model for the emissivity, we have assumed that equation (26) applies, and have adopted the case $a = 2$, which provides a spectral index of $\alpha = 0.5$ and a pressure dependence of the emissivity arising from the B-field of $P^{3/4}$. The calibration of the nonthermal flux was accomplished empirically by applying equation (23) at a pressure of $P/k = 10^4$ cm^{-3} K. The emissivity was then computed for the higher pressures, still assuming that equation (26) applies.

The result is shown in Figure 12. Here we have plotted the computed F_ν from the Lyman limit up to 30 cm (0.98 GHz). The apparent change in spectral index of the radio continuum with pressure is due to the underlying contribution of the radio free-free continuum from the ionized plasma in the H II regions. This is relatively more important at low ISM pressure. Changes in the radio nonthermal luminosity with pressure are correlated with changes in the 60 μm flux. However, it is clear that the size of the increase in the 1.4 GHz continuum computed using equation (26) is appreciably larger than the corresponding increase in the 60 μm flux. It seems clear that when the pressure of the ISM reaches $P/k \sim 10^6$ cm^{-3} K, the lifetime of the synchrotron electrons is becoming, or has become, shorter than the age of the starburst.

Once this condition is reached, then the synchrotron flux becomes more sensitive to the instantaneous injection rate of relativistic electrons. We would therefore expect more dispersion in the radio–FIR correlation at the highest pressures. Since many of the ULIRG galaxies have high pressure, this could contribute to scatter at the upper end of the radio–FIR correlation (cf. Bell 2003).

9. COMPARISON WITH OBSERVATIONS

9.1. *Pan-spectral Fits to Starburst Galaxies*

In this section we compare the theoretical SEDs with the observations of two exceedingly well observed objects; Arp 220 ($z = 0.0182$) and NGC 6240 ($z = 0.0245$). These objects are chosen because the SEDs of these objects have been established from the Lyman limit up to beyond 1000 μm. Arp 220 is widely used as the template for violent and highly extinguished starbursts and for the computation of the fluxes expected from high-redshift objects. The case of NGC 6240 (*IRAS* 16504+0228) is not so clear cut. It is a very well known ultraluminous infrared merger remnant with a strong nonthermal radio excess. It is clearly dominated by a starburst, and shows a very strong Balmer lines but has a LINER or Seyfert 2 nuclear spectrum (Kewley et al. 2001b; Goldader et al. 1997; Kim et al. 1995; Veilleux et al. 1995). It also shows evidence for an obscured AGN at X-ray and radio wavelengths (Ikebe et al. 2000; Risaliti et al. 2000; Kewley et al. 2000).

For both galaxies, the UV and optical fluxes were taken from the Third Reference Catalogue of Bright Galaxies version 3.9 (de Vaucouleurs et al. 1991). The near-IR (*JHK*-band) points are from Spinoglio et al. (1995), and include aperture corrections to allow a direct comparison with the larger aperture mid- and far-IR fluxes. The L-band magnitude for NGC 6240 (Allen 1976) has been similarly corrected by scaling with the same factor as required for the K band. The 3–1500 μm data points were taken from Klaas et al. (1997, 2001), Benford (1999), Spoon et al. (2004) and references therein. All UV to near-IR fluxes have been corrected for Galactic extinction using the $E(B-V)$ values based on *IRAS* 100 μm cirrus emission maps (Schlegel et al. 1998) and extrapolating following Cardelli et al. (1989).

The process of matching the models to the observations required two steps. First, the data were shifted to rest-frame frequencies, and the absolute flux determined from the luminosity distance of the galaxy was scaled to the FIR section of the SED. The location of the peak and the slope of the long-wavelength tail of the thermal dust re-emission fixes the appropriate value of P/k. The molecular cloud clearing timescale $\tau_{\rm clear}$ was best determined by the fit in the 2–5 μm region, which is dominated by the stellar continuum leaking out between the molecular clouds. The choice of clearing timescale also changes the inferred scaling factor in the FIR, but to a limited degree. The final scaling factor to be applied to the observed absolute fluxes is a direct measure of the star formation rate in the galaxy concerned, since all the theoretical spectra are scaled to an absolute star formation rate of 1.0 $M_\odot$ yr^{-1}. To estimate this scaling factor we assume a flat universe with $H_0 = 71$ km s^{-1} Mpc^{-1}, $\Omega_M = 0.27$, and $\Omega_\Lambda = 0.73$ (Spergel et al. 2003; Tonry et al. 2003).

Second, when a best-fit match was obtained throughout the FIR regime, the model SEDs were reddened according to the foreground turbulent screen attenuation law given in Table 3. The total attenuation was adjusted to match the integrated fluxes at optical and near-IR wavelengths. This provides a direct estimate of A_V to the star-forming region.

The full family of SEDs generated for this paper and used in this section are available in full in Table 6 in the Appendix of the electronic edition. The attenuation curves from § 6 are also given in the electronic version of the journal in the same form.

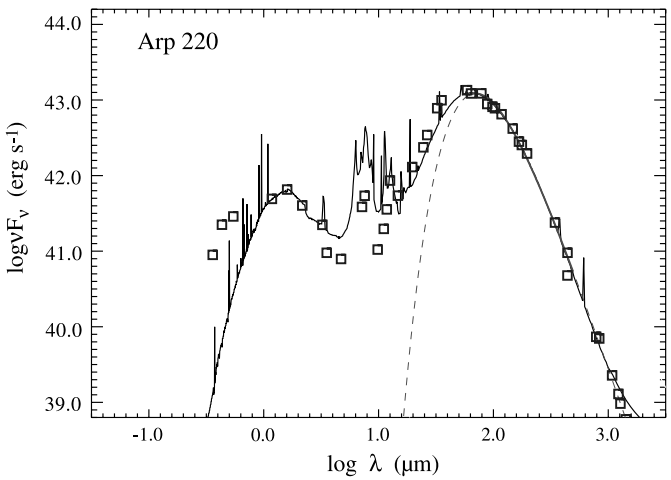

FIG. 13.—Global fit to the spectrum of Arp 220. This requires $P/k = 10^7$ cm^{-3} K, a very long clearing timescale for the molecular clouds, and a foreground dust screen with $A_V \sim 5.7$ mag. The fit implies an absolute star formation rate of 300 $M_\odot$ yr^{-1}. Also shown is the modified blackbody fit to the 60–500 μm region. [*See the electronic edition of the Journal for a color version of this figure.*]

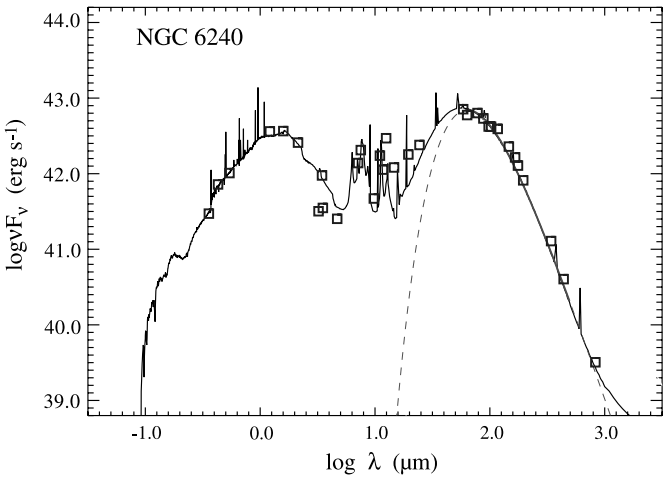

FIG. 14.—Global fit to the spectrum of NGC 6240. This requires $P/k = 10^7$ cm^{-3} K, a molecular clearing timescale $\tau_{\rm clear} \sim 8$ Myr, and $A_V = 2.7$. The fit implies an absolute star formation rate of 120 $M_\odot$ yr^{-1}. Also shown is the modified blackbody fit to the 60–500 μm region. [*See the electronic edition of the Journal for a color version of this figure.*]

In these files, and in the fitting used in this section, we have not included any synchrotron contributions, since these are so uncertain at present. Without this contribution, the model SEDs become dominated by the free-free emission (assumed optically thin) at wavelengths longer than about 2 mm.

The observed SEDs of Arp 220 and NGC 6240 with model fits overlaid are shown in Figures 13 and 14. High-pressure models with $P/k = 10^7$ cm^{-3} K were required in both cases. The SED of NGC 6240 could be accurately fitted with either a linearly decreasing covering factor or $\tau_{\rm clear} \sim 8$ Myr and with $A_V = 2.7$. However, for Arp 220 a good match to the FIR could be only be obtained for a model with $\tau_{\rm clear} = 100$ Myr. This implies that the starburst is enshrouded by an optically thick dust and molecular screen that absorbs almost all UV/optical radiation. This molecular screen effectively acts as a bolometer. The fit in the near-IR regime requires an additional attenuation of $A_V = 5.7$. It was not possible to fit the excess of flux in the UV. This component may arise from an outer stellar population, which is not as deeply dust embedded as the main star formation region. If we use the value of $N_{\rm H}/A_B - A_V = 5.8 \times 10^{21}$ cm^{-2} mag^{-1} (Bohlin et al. 1978) along with $R_V = 4.0$, then our value of $A_V \sim 5.7$ mag translates to an inferred column density of $N_{\rm H} \sim 9 \times 10^{21}$ cm^{-2}. This can be directly compared with the X-ray absorption to the nuclear source, $N_{\rm H} \sim 3 \times 10^{22}$ cm^{-2} (Clements et al. 2002). Since we would expect the central source to be more deeply dust-embedded than the more extended star formation region, our estimate of $A_V = 5.7$.

With luminosity distances of 78 and 105 Mpc for Arp 220 and NGC 6240, respectively, we infer star formation rates of 300 $M_\odot$ yr^{-1} for Arp 220 and 120 $M_\odot$ yr^{-1} for NGC 6240. As one might expect for these heavily dust-enshrouded objects, these are very close to the estimates derived from the bolometric FIR luminosities, $L_{\rm IR}$.

The fit with the observations is, in general, rather good. For Arp 220, the main differences between the data and the models are the excess in UV flux in the data, already alluded to, and a difference in the observed and predicted strength of the PAH features. The data show that the strength of the PAH features are overestimated by a factor of about 2 in the models. This difference can be understood as the result of the very high star formation rate inferred for Arp 220, which implies a strong PAH-photodissociating UV field in the star formation region. Presumably, a greater fraction of the PAHs are destroyed in this environment.

Relative to the model, Arp 220 also shows an excess of flux in the 12–30 μm band, which can be ascribed to the presence of an additional warm dust component. As discussed in § 8.1, this is most likely due to a population of confined compact and ultracompact H II regions around single OB stars, or small clusters. It is highly unlikely that this is due to the presence of an AGN, since at other wavelengths there is no evidence to support this idea.

For NGC 6240, the main difference between model and observation is that the observations also show an excess of flux in the 10–30 μm waveband. In this object, however, an AGN is undoubtedly present.

Overall, the goodness of fit over the whole range of wavelength was somewhat surprising to us. In particular, we would have expected to find a poor quality of fit in the 100–1000 μm region of the spectrum, since here the emission was thought to be dominated by the cooler dust located in the more extended dusty region surrounding the starburst, which is not represented in our modeling. However, this can be understood as a consequence of the long molecular cloud clearing timescales we inferred in the fitting procedure. This implies that the vast majority of the UV photons are being absorbed in the PDRs surrounding the H II regions. This is consistent with the rather long molecular cloud clearing timescales inferred for these objects. Because of the high pressures, these regions are very dense, and consequently thin in comparison with the radius of the H II regions. Thus, the intensity of the local radiation field is simply a function of the optical depth into the PDR. Since the local radiation field determines the local temperature, or more strictly, the temperature distribution of the dust grains, the global dust emission spectrum is a superposition of a wide range of dust temperatures. The hottest grains are located close to, or within, the ionized region, and the coolest grains are in the tail of the PDR.

Frequently, observers use a single-temperature modified blackbody spectrum as a fit to the 100–1000 μm spectra of starbursts. We have therefore generated such spectra with dust emissivity proportional to $\lambda^{-\beta}$. These have been fitted over the region 60–500 μm. Both fits yield a value $\beta = 1.5$ (similar to

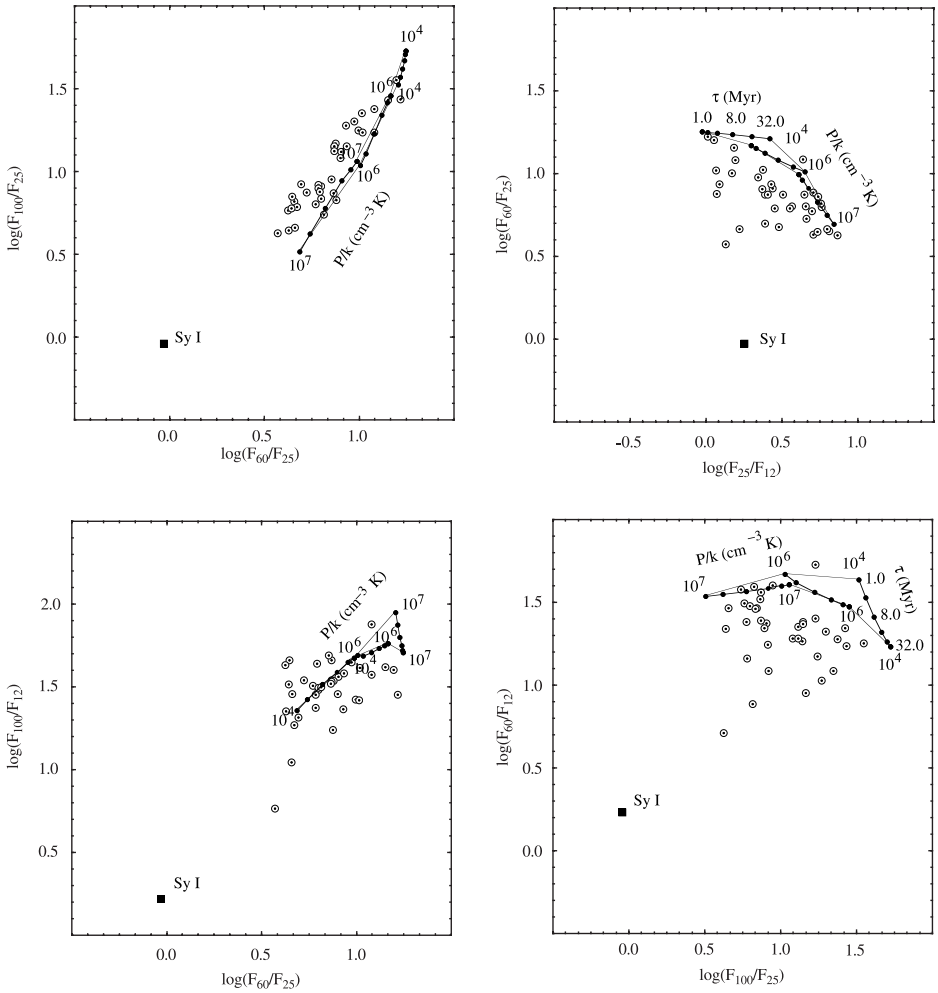

FIG. 15.—Color-color diagrams computed for the *IRAS* bands. The observational points come from the Rush et al. (1993) starbursts. The single point shows the mean colors of Seyfert 1 galaxies given by Dopita et al. (1998). Note that our models reproduce the intrinsic range of FIR colors seen in starburst galaxies, and that the grid of models in all cases defines an upper boundary around the observed points. It is clear that if the theoretical grid is correct for "pure" starbursts, then a number of the objects classified as starbursts are in fact of mixed excitation, starburst, and AGN.

what is usually assumed). The effective dust temperatures derived are $T = 37.5$ K for Arp 220 and $T = 41.3$ K for NGC 6240. This is in good agreement with what has been found for single-temperature fits to bright *IRAS* galaxies (Dunne et al. 2000). Estimates of the bolometric flux based on such parameterizations clearly underestimate the true value, since these fits do not take into account the emission at the shorter wavelengths. More complex multitemperature fits do a better job in this regard (see, e.g., Klaas et al. 2001), but all such fitting is fundamentally unphysical. Especially misleading is the use of an additional parameter, the optical depth at 100 μm. If this is misinterpreted as representing a real physical parameter, it would imply such tremendous optical depths that the starbursts would be totally invisible at optical wavelengths. Such is clearly not the case.

Nonetheless, the single-temperature fits *are* a useful way of characterizing the form of the long-wavelength side of the FIR thermal emission from dust. For example, Blain et al. (2004) have used a sample of ultraluminous galaxies in the nearby universe as well as a sample of more distant starburst galaxies ($1 < z < 5$) to find an (admittedly loose) correlation between the inferred dust temperatures and the luminosity of the host galaxy. In the framework of the theory presented here, this could be interpreted as a correlation between the star formation rate and the pressure in the ISM of the host galaxies.

9.2. *IR Color-Color Diagrams for Starburst Galaxies*

In the following sections we compute theoretical color-color diagrams for our model starbursts as would be seen using *IRAS* or *Spitzer*. We regard the computed color-color diagrams involving flux densities at wavelengths longer than 100 μm (such as those involving the *Spitzer* MIPS 160 μm filter) as unreliable. This is because we have neglected both the old stellar populations and the diffuse components of the dust, both of which are important contributors at these wavelengths for starbursts located in more normal galaxies (Popescu et al. 2000).

9.2.1. *IRAS*

We have used the bandpass data for the *IRAS* 12, 25, 60, and 100 μm bands in conjunction with our theoretical SEDs to construct color-color diagrams. These are shown in Figure 15.

Some homogeneous observational data is shown for comparison. We have used Rush et al. (1993) data for objects classified as starbursts. These are plotted as circled dots. Typical errors in this data set amount to 0.1 to 0.2 dex in terms of errors on color-color plots.

The single square represents the mean for the Rush et al. (1993) Seyfert 1 colors as determined by Dopita et al. (1998). It is clear that our theoretical curves define an upper envelope to the observed points on all four of these color-color diagrams.

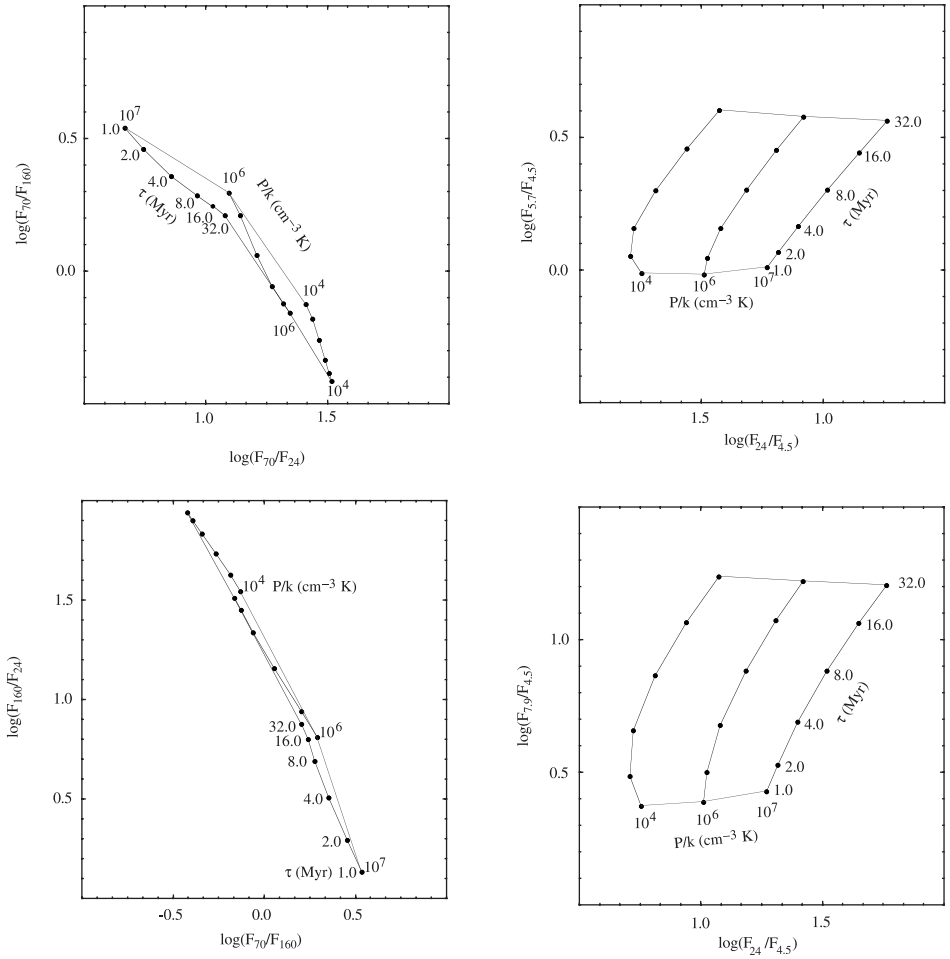

FIG. 16.—Color-color diagrams computed for the IRAC and MIPS instruments on *Spitzer*. In general, the *Spitzer* wavebands are more useful in separating the effects of ISM pressure from the time-dependent molecular cloud covering factor. Increasing pressure increases the MIPS 70 and 24 μm fluxes, but leaves the IRAC bands unchanged, while increasing covering factor decreases the stellar continuum (the IRAC 4.5 μm flux) but increases the strength of the PAH bands, most clearly in the IRAC 7.9 μm band. [*See the electronic edition of the Journal for a color version of this figure.*]

However, our detailed spectral fitting in § 9.1 shows that our models are missing a warm-dust emission component in the 12–30 μm region, which is almost certainly caused by a population of confined compact and ultracompact H II regions with ages less than about 2 Myr surrounding single OB stars or small OB clusters. This could account for the offset between the theoretical curves and the majority of the Rush et al. (1993) starbursts. However, some of the objects classified as starbursts by Rush et al. (1993) are in fact of mixed excitation, starburst+AGN. Indeed, the fact that those objects that lie particularly low on one of these color-color plots also lie low on the others makes this conclusion secure. From the mixing lines given in Dopita et al. (2004) we might infer that these objects have a bolometric contribution ascribable to the AGN of between 10% and 20% that of the starburst.

It is clear that the models reproduce the intrinsic spread in colors observed in real starburst galaxies. In general, warmer *IRAS* colors correspond to higher ISM pressures, and therefore we might expect to find a correspondence between the compactness of the starburst and its *IRAS* colors. However, none of these diagrams is suitable for separating the two controlling parameters of the ISM pressure and the molecular cloud clearing timescale.

The scatter of the points on the F_{100}/F_{25} versus F_{60}/F_{25} diagram is low. However, this can now be seen as simply a degeneracy in the parameters: both P and $\tau_{\rm clear}$ spread points in the same direction, which also happens to lie in the same direction as the AGN-starburst mixing line. The same also applies to the F_{100}/F_{12} versus F_{60}/F_{25} diagram. The remaining two color-color diagrams offer a better potential to separate the contribution of any AGN to the total spectrum, and the pressure can also be somewhat constrained.

9.2.2. *Spitzer Space Telescope*

The IRAC and MIPS instruments of the *Spitzer Space Telescope* offer the potential of observationally separating and measuring both the pressure and the molecular cloud covering factor, and also of estimating the contribution of any AGN component.

This can be done in the following manner. First, because the IRAC 4.5 μm band directly measures the stellar continuum, the 5.7 μm band sees the PAH emission, and the 7.9 μm band is completely dominated by the PAH emission, the ratio of fluxes in these wavebands is very sensitive to the covering factor.

Second, the MIPS 24 μm band is almost invariant with covering factor, but is extremely sensitive to pressure (see Figs. 9–11). Thus, the flux in this waveband can be used in conjunction with any of the IRAC bands to provide a pressure discriminant. In practice, either the IRAC 4.5 μm or the 5.7 μm bands are best for this purpose. Alternatively, longer wavelength MIPS bands could be used, but these tend to suffer the same degeneracy as the *IRAS* bands.

Finally, the presence of an AGN continuum would tend to wash out the PAH features (Laurent et al. 2000), so the ratios of fluxes in the IRAC 7.9 μm and 4.5 μm bands and any of the IRAC bands could be used to help determine the AGN fraction.

Some useful color-color plots are shown in Figure 16. This figure shows how either the $F_{5.7}/F_{4.5}$ versus $F_{24}/F_{4.5}$ or the $F_{7.9}/F_{4.5}$ versus $F_{24}/F_{4.5}$ color-color diagrams provide a clean separation between P and $\tau_{\rm clear}$, while the MIPS color-color diagrams, F_{70}/F_{160} versus F_{70}/F_{24} or F_{160}/F_{24} versus F_{70}/F_{160}, are essential degenerate in these parameters. However, by providing a starburst line on these diagrams, they can be used to help estimate the contribution of an AGN, once the mean AGN colors have been determined.

10. CALIBRATION OF STAR FORMATION RATES

10.1. *Star Formation Rates from* Hα

Neglecting the internal extinction by dust within the H II regions, the Hα flux can be fitted in terms of the molecular cloud dissipation timescale. From our models this gives, to better than 1% for $\tau \geq 2$ Myr,

$$\log\left(\frac{L_{\rm H\alpha}}{\rm ergs\ s^{-1}}\right) = 41.63 + \log\left(\frac{\rm SFR}{M_\odot\ \rm yr^{-1}}\right) - \log\left(1.6 + \frac{\tau}{\rm Myr}\right), \quad (27)$$

and for $\tau = 1$ Myr,

$$\log\left(\frac{L_{\rm H\alpha}}{\rm ergs\ s^{-1}}\right) = 41.195 + \log\left(\frac{\rm SFR}{M_\odot\ \rm yr^{-1}}\right). \quad (28)$$

For the case of $\tau = 1$ Myr, this gives the calibration for the star formation rate as

$$\frac{\rm SFR_{H\alpha}}{M_\odot\ \rm yr^{-1}} = 6.4 \times 10^{-42}\ \frac{L_{\rm H\alpha}}{\rm ergs\ s^{-1}}, \quad (29)$$

which can be compared directly with the earlier calibrations by Dopita & Ryder (1994), Kennicutt (1998), and Panuzzo et al. (2003) (cf. eq. [2]). The agreement with these earlier works is satisfactory, given the different stellar models used here and the difference in other assumptions such as the IMF. Here we require a somewhat larger Hα flux to deliver a given star formation rate. However, it should be emphasized that for other values of the molecular cloud dissipation timescale, equation (27) should be used, and these will require a greater star formation rate to produce a given Hα flux.

10.2. *Star Formation Rates from the UV and GALEX*

The *GALEX* satellite offers two wavebands centered at 1500 Å (FUV) and 2200 Å (NUV). We have folded the response function of these bandpasses with our predicted FUV SED. As can be seen from Figure 8, the SED is unaffected by the ISM pressure. Instead, it is strongly influenced by the molecular cloud clearing timescale. This is because, to first order, the molecular clouds act to obscure some fraction of the exciting stars. Since, for any particular star, this obscuration is either nonexistent or total, the attenuation produced by the molecular clouds is effectively wavelength independent. The small changes in the slope of the FUV spectrum, and in the relative intensity of particular spectral features in the UV, apparent in Figure 10, are produced by age differences in the observable stellar populations. In regions with long molecular cloud clearing timescales, the younger stars tend to be preferentially obscured.

In real starburst galaxies, the FUV spectrum will also be obscured by the overlying foreground screen of material. We assume that this can be described by the attenuation curve given in Figure 5 and Table 3. Here we are concerned only with the conversion of the absolute UV flux to star formation rate.

We find that for the model starbursts, the *GALEX* 1500 and 2200 Å bands provide nearly the same flux, $F(1500)/F(2200) = 1.03 \pm 0.015$, for all values of the molecular cloud dissipation timescale. The $F(1500)$ flux can be fitted, like the Hα flux in terms of the molecular cloud dissipation timescale. For all computed values of τ, this is given to better than 3% accuracy by

$$\log\left(\frac{L_{1500}}{\rm ergs\ s^{-1}\ Hz^{-1}}\right) = 28.62 + \log\left(\frac{\rm SFR}{M_\odot\ \rm yr^{-1}}\right) - \log\left(2.3 + 0.37\frac{\tau}{\rm Myr}\right).$$

This flux accounts for the internal dust extinction (or, more properly, attenuation) of the H II regions, but it does not account for any foreground screen attenuation.

The dependence of the flux on τ is weaker than for Hα because the Hα flux is produced mostly in the first 4–5 Myr of a starburst, and so is very prone to obscuration by the placental molecular clouds of the starburst itself. In contrast, the stellar UV flux at 1500 Å remains appreciable out to an age of tens of Myr and so is much less affected. Indeed, because of this, the computed $F(1500)$ flux is somewhat sensitive to the assumed duration of the starburst, with older stars contributing significantly to the UV flux at this wavelength. For example, with $\tau = 1$ Myr, a 1.0 $M_\odot\ \rm yr^{-1}$ starburst continued for 10^8 yr will give and absolute flux $F(1500) = 1.58 \times 10^{28}$ ergs s^{-1} Hz^{-1}. However, if the duration of the starburst is only 10^7 yr, the UV flux falls to $F(1500) = 1.04 \times 10^{28}$ ergs s^{-1} Hz^{-1}.

For comparison with earlier calibrations, for a 10^7 yr duration starburst with a molecular cloud dissipation timescale, $\tau = 1$ Myr,

$$\frac{\rm SFR_{UV}}{M_\odot\ \rm yr^{-1}} = 0.96 \times 10^{-28}\ \frac{L_{1500}}{\rm ergs\ s^{-1}\ Hz^{-1}}. \quad (30)$$

Again, we require a larger observed L_{1500} flux to deliver a given star formation rate, but larger values of the molecular cloud dissipation timescale require a greater star formation rate to produce a given L_{1500} flux.

10.3. *Star Formation Rates from the FIR*

In the FIR, fluxes are affected by both the pressure and the molecular dissipation timescale, so the situation with respect to determining star formation rates is somewhat complex. If we were to choose a single wavelength for which the effect of the molecular dissipation timescale is largely compensated, then we would choose the *IRAS* 25 μm or the *Spitzer* MIPS 24 μm band. This is because at this wavelength, the reduction in the strength of the PAH bands for shorter molecular dissipation timescales is compensated by the increasing color temperature of the FIR re-emission continuum (see Figs. 9, 10, and 11). This waveband probably gives the most reliable conversion of flux to star formation rate when τ is not known. In Table 4 we give the computed luminosities through the MIPS 24 μm band and

TABLE 4
MODEL *Spitzer* AND *IRAS* 25 μm LUMINOSITIES

τ (Myr)	P/k 10^4	10^6	10^7
	log $L_{\rm MIPS(24\ \mu m)}$		
1	7.395	7.676	7.952
2	7.331	7.676	7.976
4	7.288	7.683	8.000
8	7.271	7.694	8.022
16	7.267	7.706	8.039
32	7.268	7.714	8.049
	log $L_{\rm IRAS(25\ \mu m)}$		
1	7.739	8.003	8.245
2	7.682	8.006	8.269
4	7.645	8.014	8.295
8	7.631	8.026	8.324
16	7.630	8.038	8.337
32	7.630	8.046	8.348

NOTE.—Given in terms of $\log L/L_\odot$ units for a star formation rate of 1.0 $M_\odot$ yr^{-1}, as a function of both τ and P/k.

TABLE 5
MODEL *IRAS* IR AND FIR LUMINOSITIES

τ (Myr)	P/k 10^4	10^6	10^7
	log $L_{\rm FIR}$		
1	9.131	9.164	9.063
2	9.111	9.200	9.155
4	9.096	9.263	9.261
8	9.103	9.329	9.342
16	9.116	9.380	9.450
32	9.127	9.405	9.496
	log $L_{\rm IR}$		
1	9.375	9.444	9.471
2	9.379	9.525	9.536
4	9.402	9.556	9.616
8	9.443	9.626	9.686
16	9.478	9.681	9.758
32	9.501	9.707	9.793

NOTE.—Given in terms of $\log L/L_\odot$ units for a star formation rate of 1.0 $M_\odot$ yr^{-1}, as a function of τ and P/k.

the *IRAS* 25 μm band for a star formation rate of 1.0 $M_\odot$ yr^{-1}. With this star formation rate, these IR luminosities can be fitted to an accuracy of $\pm 15\%$, which is probably sufficient for most astronomical purposes, by a simple function of pressure, $\log\left(L_{25\mu\rm m}/L_\odot\right) = f(P/k)$, with $f(P/k) = 7.30$, 7.69, and 8.00 (MIPS) and 7.66, 8.02, and 8.30 (*IRAS*) for the three pressures $P/k = 10^4$,10^6, and 10^8, respectively.

More usually, we are accustomed to using the conversion between FIR luminosity $L_{\rm FIR}$, or the total IR luminosity $L_{\rm IR}$. For the *IRAS* wavebands these are defined by Saunders & Mirabel (1996) as

$$L_{\rm FIR} = 2.58 L_{60\mu\rm m} + L_{100\mu\rm m} \tag{31}$$

and

$$L_{\rm IR} = 13.48 L_{12\mu\rm m} + 5.16 L_{25\mu\rm m} + 2.58 L_{60\mu\rm m} + L_{100\mu\rm m}. \tag{32}$$

With these definitions, we have computed the model fluxes for a star formation rate of 1.0 $M_\odot$ yr^{-1}. These are given in Table 5. There is no simple fit to these luminosities, owing to the sensitivity to τ, particularly at the larger values of P/k.

When τ is long, and the pressure is high, then the majority of the stellar flux is reradiated in the FIR, and $L_{\rm IR}$ becomes a good measure of the bolometric luminosity of the exciting stars. This is particularly true at high pressure, since the dust temperature is then high enough that the emission beyond 100 μm becomes unimportant. Put another way, the dust shell is virtually complete around the stars, and so the dust shell acts as an IR bolometer. For the most extreme case computed ($\tau = 32$ Myr, $P/k = 10^7$ cm^{-3} K), $L_{\rm IR}$ provides a conversion to star formation that can be compared with earlier estimates by Kennicutt (1998) and Panuzzo et al. (2003) (see eq. [3]),

$$\frac{\rm SFR_{IR}}{M_\odot\ \rm yr^{-1}} = 4.2 \times 10^{-44} \frac{L_{\rm IR}}{\rm ergs\ s^{-1}}\ . \tag{33}$$

This agrees well with these earlier estimates. However, in general the dust shell will be more incomplete, and a greater fraction of luminosity is emitted longward of the 100 μm band, so that the numerical factor in equation (33) will be larger. From Table 4 we find that it can range up to 11×10^{-44}, so that star formation estimates using equation (3) may underestimate the star formation rate by a factor of over 2 in certain circumstances.

11. CONCLUSIONS

In this paper we have attempted to provide a self-consistent theoretical modeling of the pan–spectral energy distribution of starbursts within the context of a simplified one-dimensional evolutionary model of their component H II regions. Although this modeling is rather more sophisticated than many models presented hitherto, it still suffers from a number of important limitations, which we feel should imply a *caveat emptor* to the hopeful observer who would like to use the results presented here. Enumerating these limitations:

1. The clusters are treated as having a single characteristic mass, 10^4 $M_\odot$, rather than being distributed over all possible masses.
2. The one-dimensional model H II evolution is oversimplified, as it does not take into account mixing and dynamical instabilities, which certainly will occur in two dimensions, nor does it take into account the intrinsic inhomogeneities in the surrounding ISM. These effects have been incorporated in a "correction factor," which reduces the efficiency of the stellar winds in inflating the surrounding bubble of ionized gas, and its magnitude is chosen so as to provide ionization parameters $\mathcal{U}$ in the range observed. Since $\mathcal{U}$ also determines the dust temperature in the surrounding shell, this choice of the correction also ensures that our computed dust temperatures in the molecular shells are more or less correct.
3. We appear to be missing a population of compact and ultracompact H II regions around single OB stars or small OB clusters. These will provide an excess of flux in the 10–30 μm

band, and would allow a better match to the observed SEDs of starbursts and to the observed color-color diagrams.

4. The dynamical evolution of the central cluster is not taken into account. This will alter the geometry of the stars with respect to the molecular gas, and would lead to different dust temperature distributions and different effective covering factors of the molecular gas, f, as a function of time. This effect will become more important at high P/k because the H II region expansion "stalls" at an earlier phase of its evolution.

5. Collective effects are not taken into account. That is to say, we have not considered mutual overlap of H II regions along the line of sight, such as certainly occurs in very dense starbursts such as Arp 220. The treatment of such cases would require the SEDs computed here to be input as source functions into a complex dust radiative transfer code, such as used by Popescu et al. (2000).

6. The diffuse component of the dust has only been included with respect to the attenuation of stellar light. The emission from this dust, which is expected to become dominant beyond 100 μm (Popescu et al. 2000), is not considered. Furthermore, old stars, that is to say stars older than 10^8 yr, have not been included. As well as providing an additional component of direct light in the visual/near-IR spectral range, these stars are also important in powering the diffuse dust emission component.

7. Observations of starburst galaxies, e.g. Meurer et al. (1999) and Calzetti (2001), show that in the visible and UV, much of the wavelength-dependent attenuation by dust can be understood as due to a foreground diffuse screen of material. Much of this dust would have to lie outside the main star-forming region. In our models we do not take this material into account, although we have provided the expected attenuation properties of this material in Table 3. This material may well provide an important contribution to the FIR dust continuum beyond 100 μm, and would again have to be accounted for within a full galactic dust radiative transfer code.

Despite these limitations, these models may well prove useful in providing SED templates for individual star formation regions within normal galaxies or for starburst galaxies that do not contain an important old star population, or in which there is no extended diffuse dust component. For this reason, the computed SEDs (Table 6), the attenuation functions (Table 8), and the filter transmissions (Table 7; sampled at the same frequencies) for the various space missions referred to in this paper are available in full in the Appendix of the electronic version of the journal.

Despite the limitations listed above, this work provides a number of important advances:

1. We have demonstrated how the dust attenuation law of Calzetti (2001) for starburst galaxies can arise as a natural consequence of turbulence on photochemistry in the diffuse phases of the ISM. In an earlier paper, Fischera et al. (2003) showed how the large values of R_V observed in starburst galaxies arise naturally from the lognormal column density distribution imposed on the diffuse ISM by turbulent processes. In that work, the observed absence of a 2200 Å dust absorption feature remained unexplained. Here we have shown that, if most of the interstellar carbon is locked up into PAHs rather than graphitic or amorphous organic grains, then the photodissociation of the PAHs in the strong UV radiation fields of starburst galaxies can explain the weakness of the 2200 Å feature in absorption, while preserving the strong IR PAH emission features originating from the photodissociation regions of molecular clouds.

2. We have demonstrated that two ISM parameters control the form of the SEDs: the pressure in the diffuse phase of the ISM (or, equivalently, the density), and the molecular cloud dissipation timescale. Long dissipation timescales for the molecular clouds enhance the PAH IR emission features by increasing the molecular cloud covering factors, but serve to obscure the central clusters in the visible and the UV. High pressures put the dense dusty gas closer to the exciting stars, giving higher stochastic dust grain temperatures.

3. We have demonstrated that the models are capable of describing the SED of well-observed starbursts over more than three decades of frequency, and we have shown that bolometrically based star formation rate estimates and foreground dust attenuations can be easily derived from this fitting.

4. We have shown that the models reproduce the observed *IRAS* colors and range of colors for starburst galaxies, and we have provided diagnostic color-color plots for the *Spitzer* MIPS and IRAC instruments, which offer the potential to solve for the two controlling parameters of the SED.

5. We have provided fitting formulae or tables to enable the conversion of observed fluxes to star formation rates in the UV (*GALEX*), at optical wavelengths (Hα), and in the IR (*IRAS* or *Spitzer*) We have shown that the 25 μm fluxes are particularly valuable as star formation indicators, since they depend little on the molecular gas dissipation timescale, and only weakly on the ISM pressure.

Notwithstanding the limitations of these models, we hope that these results have been presented in such a way as to be useful for observers who are seeking both to understand star formation in galaxies, and in the universe at large.

M. Dopita acknowledges the support of both the Australian National University and of the Australian Research Council (ARC) through his ARC Australian Federation Fellowship. He would also like to thank Huub Röttgering for organizing his visit to Sterrewacht Leiden, where this work was started. M. Dopita, R. Sutherland, and J. Fishera recognize the financial support of the ARC through Discovery Project grant DP0208445. M. Reuland acknowledges the support of a travel grant through M. Dopita's ARC Australian Federation Fellowship Support grant. L. Kewley is supported by a Harvard-Smithsonian CfA Fellowship. This research has made use of the NASA/IPAC Extragalactic Database (NED), which is operated by the Jet Propulsion Laboratory, California Institute of Technology, under contract to NASA. Finally, all of us wish to thank the anonymous referee whose careful reading of the manuscript and helpful suggestions has led to a much clearer end product.

APPENDIX

Tables 6, 7, and 8 are provided as supplementary to the paper. They are published in their entirety in the electronic edition of the *Astrophysical Journal*; a portion is shown here for guidance regarding their form and content.

TABLE 6

MODEL STARBURST SEDs

ν (Hz)	λ (μm)	$\nu f(\nu)$ 1 Myr	2 Myr	4 Myr	8 Myr	16 Myr	32 Myr	Linear
		$P/k = 1E4$, $\tau = 1-32$ Myr						
3.68697E+08	813112	2.0E+36	1.9E+36	1.8E+36	1.7E+36	1.7E+36	1.6E+36	1.7E+36
4.03155E+08	743615	4.8E+36	5.5E+36	6.3E+36	6.9E+36	7.4E+36	7.6E+36	7.0E+36
4.40833E+08	680058	3.1E+42	3.5E+42	4.1E+42	4.6E+42	5.0E+42	5.2E+42	4.6E+42
4.82032E+08	621934	2.6E+36	2.4E+36	2.3E+36	2.2E+36	2.2E+36	2.1E+36	2.2E+36
5.27082E+08	568777	1.5E+37	1.6E+37	1.8E+37	2.0E+37	2.1E+37	2.1E+37	2.0E+37

TABLE 7

GALEX, *IRAS*, AND *Spitzer* FILTER FUNCTIONS

ν	λ	*GALEX*		*IRAS*				IRAC				MIPS		
(Hz)	(μm)	1500 Å	2300 Å	100 μm	60 μm	25 μm	12 μm	3.5 μm	4.5 μm	5.7 μm	7.9 μm	160 μm	70 μm	24 μm
2.13E+12	141.0174595	0	0	0.01	0	0	0	0	0	0	0	0.608 0	0	
2.17E+12	138.2524105	0	0	0.035	0	0	0	0	0	0	0	0.4222 0	0	
2.21E+12	135.5415825	0	0	0.05	0	0	0	0	0	0	0	0.2936 0	0	
2.28E+12	131.5131153	0	0	0.085	0	0	0	0	0	0	0	0.17 0	0	
2.35E+12	127.7147177	0	0	0.146	0	0	0	0	0	0	0	0.0712 0	0	

TABLE 8

ATTENUATION CURVE FOR THE MODELS PRESENTED IN THE PAPER

λ (μm)	$E(\lambda-V)/E(B-V)$
1000.00	−4.0269432
988.600	−4.0269416
977.200	−4.0269400
966.100	−4.0269384
955.000	−4.0269368

REFERENCES

Adelberger, K. L., & Steidel, C. C. 2000, ApJ, 544, 218
Allain, T., Leach, S., & Sedlmayr, E. 1996a, A&A, 305, 602
———. 1996b, A&A, 305, 616
Allamandola, L. J., Hudgins, D. M., & Sandford, S. A. 1999, ApJ, 511, L115
Allen, D. A. 1976, ApJ, 207, 367
Allende Prieto, C., Lambert, D. L., & Asplund, M. 2001, ApJ, 556, L63
———. 2002, ApJ, 573, L137
Asplund, M. 2000, A&A, 359, 755
Asplund, M., Nordlund, A., Trampedach, R., & Stein, R. F. 2000, A&A, 359, 743
Barnes, J. E., & Hernquist, L. 1996, ApJ, 471, 115
Barton, B. J., Geller, M. J., & Kenyon, S. J. 2000, ApJ, 530, 660
Bell, E. F. 2003, ApJ, 586, 794
Bell, E. F., & Kennicutt, R. C., Jr. 2001, ApJ, 548, 681
Benford, D. J. 1999, Ph.D. thesis, California Institute of Technology
Blain, A. W., Chapman, S. C., Smail, I., & Ivison, R. 2004, ApJ, 611, 52
Bohlin, R. C., Savage, B. D., & Drake, J. F. 1978, ApJ, 224, 132
Bottorff, M., LaMothe, J., Momjian, E., Verner, E., Vinkovič, D., & Ferland, G. 1998, PASP, 110, 1040
Boulanger, F., Boissel, P., Cesarsky, D., & Ryter,C. 1998, A&A, 339, 194
Bressan, A., Silva, L., & Granato, G. L. 2002, A&A, 392, 377
Burton, M. G., et al. 2000, ApJ, 542, 359
Bushouse, H. A. 1987, ApJ, 320, 49
Calzetti, D. 2001, PASP, 113, 1449
Cardelli, J. A., Clayton, G. C., & Mathis, J. S. 1989, ApJ, 345, 245
Cho, J., & Vishniac, E. T. 2000b, ApJ, 539, 273
Clements, D. L., McDowell, J. C., Shaked, S., Baker, A. C., Borne, K., Colina, L., Lamb, S. A., & Mundell, C. 2002, ApJ, 581, 974
Condon, J. J. 1992, ARA&A, 30, 575
Condon, J. J., Condon, M. A., Gisler, G., & Puschell, J. J. 1982, ApJ, 252, 102
Condon, J. J., & Dressel, L. L. 1978, ApJ, 221, 456
Dale, D. A., & Helou, G. 2002, ApJ, 576, 159
Dale, D. A., Helou, G., Contursi, A., Silberman, N. A., & Kolhatkar, S. 2001, ApJ, 549, 215
de Vaucouleurs, G., de Vaucouleurs, A., Corwin, H. G., Buta, R. J., Paturel, G., & Fouque, P. 1991, Third Reference Catalogue of Bright Galaxies (Berlin: Springer)
Donzelli, C. J., & Pastoriza, M. G. 1997, ApJS, 111, 181
Dopita, M. A., Fischera, J., Groves, B., Sutherland, R. S., Kewley, L. J., Tuffs, R., Popescu, C., & Leitherer, C. 2004, in Proc. IAU Symp. 222, The Interplay among Black Holes, Stars and ISM in Galactic Nuclei, ed. T. Storchi-Bergmann (Cambridge: Cambridge Univ. Press), in press
Dopita, M. A., Groves, B. A., Sutherland, R. S., Binette, L., & Cecil, G. 2002a, ApJ, 572, 753
Dopita, M. A., Groves, B. A., Sutherland, R. S., & Kewley, L. J. 2003, ApJ, 583, 727
Dopita, M. A., Heisler, C. A., Lumsden, S., & Bailey, J. 1998, ApJ, 498, 570
Dopita, M. A., Kewley, L. J., Heisler, C. A., & Sutherland, R. S. 2000, ApJ, 542, 224
Dopita, M. A., Pereira, M., Kewley, L. J., & Capaccioli, M. 2002b, ApJS, 143, 47
Dopita, M. A., & Ryder, S. D. 1994, ApJ, 430, 163
Dopita, M. A., & Sutherland, R. S. 2003, Diffuse Matter in the Universe (Heidelberg: Springer)
Draine, B. T., & Anderson, N. 1985, ApJ, 292, 494
Draine, B. T., & Li, A. 2001, ApJ, 551, 807
Duley, W. W. 1973, Ap&SS, 23, 43
Dunne, L., Eales, S., Edmunds, M., Ivison, R., Alexander, P., & Clements, D. L. 2000, MNRAS, 315, 115
Dwek, E. 1986, ApJ, 302, 363
Dwek, E., et al. 1998, ApJ, 508, 106
Fischera, J., Dopita, M. A., & Sutherland, R. S. 2003, ApJ, 599, L21
Gallego, J., Zamorano, J., Aragón-Salamanca, A., & Rego, M. 1995, ApJ, 455, L1
García-Segura, G., & Mac Low, M.-M. 1995, ApJ, 455, 160
Gispert, R., Lagache, G., & Puget, J. L. 2000, A&A, 360, 1
Goldader, J. D., Joseph, R. D., Doyon, R., & Sanders, D. B. 1997, ApJ, 474, 104
Granato, G. L., Lacey, C. G., Silva, L., Bressan, A., Baugh, C. M., Cole, S., & Frenk, C. S. 2000, ApJ, 542, 710
Greenberg, J. M., & Hong, S.-S. 1974, IAU Symp. 60, Galactic Radio Astronomy (Dordrecht: Reidel), 155
Groves, B. A., Cho, J., Dopita, M., & Lazarian, A. 2003, Publ. Astron. Soc. Australia, 20, 252
Guhathakurta, P., & Draine, B. T. 1989, ApJ, 345, 230
Haas, M., Lemke, D., Stickel, M., Hippelein, H., Kunkel, M., Herbstmeier, U., & Mattila, K. 1998, A&A, 338, L33
Hillier, D. J., & Miller, D. L. 1998, ApJ, 496, 407
Hippelein, H., Haas, M., Tuffs, R. J., Lemke, D., Stickel, M., Klaas, U., & Völk, H. J. 2003, A&A, 407, 137
Hirashita, H., Buat, V., & Inoue, A. K. 2003, A&A, 410, 83
Hirashita, H., & Ferrara, A. 2002, MNRAS, 337, 921
Hummel, E. 1980, A&A, 89, L1
Hummel, E., van der Hulst, J. M., Kennicutt, R. C., & Keel, W. C. 1990, A&A, 236, 333
Ikebe, Y., Leighly, K., Tanaka, Y., Nakagawa, T., Terashima, Y., & Komossa, S. 2000, MNRAS, 316, 433
Inoue, A. K. 2001, AJ, 122, 1788
———. 2002, ApJ, 570, L97
Inoue, A. K., Hirashita, H., & Kamaya, H. 2000, PASJ, 52, 539
———. 2001, ApJ, 555, 613
Jenkins, E. B. 1983, in Kinematics, Dynamics and Structure of the Milky Way (Dordrecht: Reidel), 21
Jenkins, E. B., Jura, M., & Loewenstein, M. 1983, ApJ, 270, 88
Jones, A. P., Tielens, A. G. G. M., & Hollenbach, D. J. 1996, ApJ, 469, 740
Jones, D. H., & Bland-Hawthorn, J. 2001, ApJ, 550, 593
Keel, W. C., Kennicutt, R. C., Hummel, E., & van der Hulst, J. M. 1985, AJ, 90, 708
Kennicutt, R. C., Jr. 1998, ARA&A, 36, 189
Kennicutt, R. C., Roettiger, K. A., Keel, W. C., van der Hulst, J. M., & Hummel, E. 1987, AJ, 93, 1011
Kewley, L. J., & Dopita, M. A. 2002, ApJS, 142, 35
Kewley, L. J., Dopita, M. A., Sutherland, R. S., Heisler, C. A., & Trevena, J. 2001a, ApJ, 556, 121
Kewley, L. J., Heisler, C. A., Dopita, M. A., & Lumsden, S. 2001b, ApJS, 132, 37
Kewley, L. J., Heisler, C. A., Dopita, M. A., Sutherland, R. S., Norris, R., Reynolds, J., & Lumsden, S. 2000, ApJ, 530, 704
Kim, D.-C., Sanders, D. B., Veilleux, S., Mazzarella, J. M., & Soifer, B. T. 1995, ApJS, 98, 129
Klaas,U., Haas, M., Heinrichsen, I., & Schulz, B. 1997, A&A, 325, L21
Klaas, U., et al. 2001, A&A, 379, 823
Kurucz, R. L. 1992, in IAU Symp. 149, The Stellar Populations of Galaxies, ed. B. Barbuy & A. Renzini (Dordrecht: Kluwer), 225
Lambas, D. G., Tissera, P. B., Sol Alonso, M., & Coldwell, G. 2003, MNRAS, 346, 1189
Larson, R. B., & Tinsley, B. M. 1978, ApJ, 219, 46
Laurent, O., Mirabel, I. F., Charmandaris, V., Gallais, P., Madden, S. C., Sauvage, M., Vigroux, L., & Cesarsky, C. 2000, A&A, 359, 887
Léger, A., & Puget, J. L. 1984, A&A, 137, L5
Leitherer, C., et al. 1999, ApJS, 123, 3
Lejeune, Th., Cuisinier, F., & Buser, R. 1997, A&AS, 125, 229
Li, A., & Draine, B. T. 2001, ApJ, 554, 778
Madau, P., Ferguson, H. V. C., Dickinson, M. E., Giavalisco, M., Steidel, C. C., & Fruchter, A. 1996, MNRAS, 283, 1388
Madore, B. F. 1986, in Spectral Evolution of Galaxies, ed. C. Chiosi & A. Renzini (Dordrecht: Reidel), 97
Mathis, J. S., Rumpl, W., & Nordsieck, K. H. 1977, ApJ, 217, 425 (MRN)
Meurer, G. R., Heckman, T. M., & Calzetti, D. 1999, ApJ, 521, 64
Meurer, G. R., Heckman, T. M., Lehnert, M. D., Leitherer, C., & Lowenthal, J. 1997, AJ, 114, 54
Mezger, P. G., Smith, L. F., & Churchwell, E. 1974, A&A, 32, 269
Misiriotis, A., Popescu, C. C., Tuffs, R. J., & Kylafis, N. D. 2001, A&A, 372, 775
Moorwood, A. F. M, van der Werf, P. P., Cuby, J. G., & Oliva, E. 2000, A&A, 362, 9
Natta, A., & Panagia, N. 1976, A&A, 50, 191
Nazé, Y., Chu, Y.-H., Points, S. D., Danforth, C. W., Rosado, M., & Chen, C.-H. R. 2001, AJ, 122, 921
Niklas, S., Klein, U., & Wielebinski, R. 1997, A&A, 322, 19
Oey, M. S. 1996, ApJ, 467, 666
Oey, M. S., & Clarke, C. J. 1997, MNRAS, 289, 570
———. 1998, AJ, 115, 1543
Panagia, N. 1974, ApJ, 192, 221
Panuzzo, P., Bressan, A., Granato, G. L., Silva, L., & Danese, L. 2003, A&A, 409, 99
Pascual, S., Gallego, J., Aragón-Salamanca, A., & Zamorano, J. 2001, A&A, 379, 798
Pauldrach, A. W. A., Hoffmann, T. L., & Lennon, M. 2001, A&A, 375, 161
Peeters, E. 2002, PhD. thesis, Rijksuniversiteit Groningen
Petrosian, A., McLean, B., Allen, R. J., Leitherer, C., MacKenty, J., & Nino, P. 2002, AJ, 123, 2280
Petrosian, A. R., Saakian, K. A., & Khachikian, E E. 1978, Astrofizika, 14, 69
Petrosian, V., Silk, J., & Field, G. B. 1972, ApJ, 177, L69
Pierini, D., Popescu, C. C., Tuffs, R. J., & Völk, H. J. 2003, A&A, 409, 907

Popescu, C. C., Misiriotis, A., Kylafis, N. D., Tuffs, R. J., & Fischera, J. 2000, A&A, 362, 138
Popescu, C. C., Tuffs, R. J., Kylafis, N. D., & Madore, B. F. 2004, A&A, 414, 45
Popescu, C. C., Tuffs, R. J., Völk, H. J., Pierini, D., & Madore, B. F. 2002, ApJ, 567, 221
Purcell, E. M. 1976, ApJ, 206, 685
Risaliti, G., Gilli, R., Maiolino, R., & Salvati, M. 2000, A&A, 357, 13
Rush, B., Malkan, M. A., & Spinoglio, L. 1993, ApJS, 89, 1
Sarazin, C. L. 1977, ApJ, 211, 772
Saunders, D. B., & Mirabel, I. F. 1996, ARA&A, 34, 749
Savage, B. D., & Sembach, K. R. 1996, ARA&A, 34, 279
Sawicki, M., & Yee, H. K. C. 1998, AJ, 115, 1329
Schlegel, D. J., Finkbeiner, D. P., & Davis, M. 1998, ApJ, 500, 525
Sersic, J. L., & Pastoriza, M. 1967, PASP, 79, 152
Shields, J. C., & Kennicutt, R. C. 1995, ApJ, 454, 807
Silva, L., Granato, G. L., Bressan, A., & Danese, L. 1998, ApJ, 509, 103
Smith, L. F., Biermann, P., & Mezger, P. G. 1978, A&A, 66, 65
Smith, L. J., Norris, R. P. F., & Crowther, P. A. 2002, MNRAS, 337, 1309
Spergel, D. N., et al. 2003, ApJS, 148, 175
Spinoglio, L., Malkan, M. A., Rush, B., Carrasco, L., & Recillas-Cruz, E. 1995, ApJ, 453, 616
Spoon, H. W. W., Moorwood, A. F. M., Lutz, D., Tielens, A. G. G. M., Siebenmorgen, R., & Keane, J. V. 2004, A&A, 414, 873
Sulentic, J. W. 1976, ApJS, 32, 171
Sutherland, R. S., & Dopita, M. A. 1993, ApJS, 88, 253
Tagaki, T., Arimoto, N., & Hanami, H. 2003a, MNRAS, 340, 813
Tagaki, T., Vansevicius, V., & Arimoto, N. 2003b, PASJ, 55, 385
Takeuchi, T. T., Hirashita, H., Ishii, T. T., Hunt, L. K., & Ferrara, A. 2003, MNRAS, 343, 839
Tonry, J. L., et al. 2003, ApJ, 594, 1
Trager, S. C., Faber, S. M., Dressler, A., & Oemler, A., Jr. 1997, ApJ, 485, 92
Tresse, L., & Maddox, S. J. 1998, ApJ, 495, 691
Tuffs, R. J., & Popescu, C. C. 2003, in Exploiting the *ISO* Data Archive: Infrared Astronomy in the Internet Age, ed. C. Gry et al. (ESA SP-511; Noordwijk: ESA), 239
Tuffs, R. J., Popescu, C. C., Völk, H. J., Kylafis, N. D., & Dopita, M. A. 2004, A&A, 419, 821
Van Kerckhoven, C., et al. 2000, A&A, 357, 1013
Veilleux, S., Kim, D.-C., Sanders, D. B., Mazzarella, J. M., & Soifer, B. T. 1995, ApJS, 98, 171
Verstraete, L., et al. 2001, A&A, 372, 981
Vorontsov-Velyaminov, B. A. 1959, Atlas and Catalogue of Interacting Galaxies (Moscow: Moscow State Univ.)
Weaver, R., McCray, R., Castor, J., Shapiro, P., & Moore, R. 1977, ApJ, 218, 377
Weingartner, J. C., & Draine, B. T. 2001, ApJ, 548, 296
Wunderlich, E., Wielebinski, R., & Klein, U. 1987, A&AS, 69, 487
Yan, L., McCarthy, P. J., Freudling, W., Teplitz, H. J., Malumuth, E. M., Weymann, R. J., & Malkan, M. A. 1999, ApJ, 519, L47
Yun, M. S., Reddy, N. A., & Condon, J. J. 2001, ApJ, 554, 803